SCUOLA DI SCIENZE
Dipartimento di Chimica Industriale "Toso Montanari"

Corso di Laurea Magistrale in
Chimica Industriale
Curriculum: Advanced Spectroscopy in Chemistry
Classe LM-71 - Scienze e Tecnologie per la Chimica Industriale

Synthesis, Characterisation and Electrochemical study of Titanium Hexacyanoferrate

Electrode material

CANDIDATE

Min Li

SUPERVISOR

Prof. Marco Giorgetti

CO-SUPERVISOR

Dott. Angelo Mullaliu

Session I

Academic Year 2018/2019

Contents

Abstract

Titanium Hexacyanoferrate (TiHCF) was synthesized by simple co-precipitation method, and the crystal structure, water content, chemical formula and a deep structural investigation (local geometry of Ti) of as-prepared sample were done by PXRD, FT-IR, TGA, MP-AES and XAS. Electrochemical tests were performed both in glass and coin cells. From cyclic voltammetry curves, we observed redox peaks of both $Fe^{3+/2+}$ and $Ti^{4+/3+}$ pairs. The calculation result based on scan rate and current shows that the capacity of battery is controlled by diffusion process in aqueous electrolyte system. The as-prepared sample also shows high performance in organic electrolyte system. Compared to Li-ion batteries, the material shows high capacity for Na-ion batteries with 74 mAh/g at C/20 rate, while Li-ion batteries only have 35 mAh/g. The specific energy value we got for Na-ion coin cell is 250 Wh/kg (based on the mass of active material) and 122 Wh/kg for Li-ion coin cell. Both Li- and Na- half cells display high coulombic efficiency during cyclability test, above 95%.

Keywords: Titanium Hexacyanoferrate, Cathode material, Aqueous electrolyte, Organic electrolyte

I. Introduction

1.1Study background

With the increasing world population, as well as increasing per capita energy consumption, worldwide energy consumption has been increasing rapidly. The impact of this growth in energy consumption on the environment and society is becoming more and more apparent. And this has accelerated the development and deployment of renewable energy sources (RES) harvesting technologies and facilities. Meanwhile the increase of RES has highlighted the next big challenge: storage of energy when demand is lower than the supply. Several energy storage technologies exist, many of which have been used for decades, as show in figure1 [1]. Among the different technologies, pump-hydro and compressed-air energy storage are widely used, but both have serious infrastructure requirements that limit large-scale energy storage to specific sites [2]. Batteries have the highest cost reduction potential at this moment. And rechargeable Lithium-ion batteries (LIBs) are the leading option for this application.

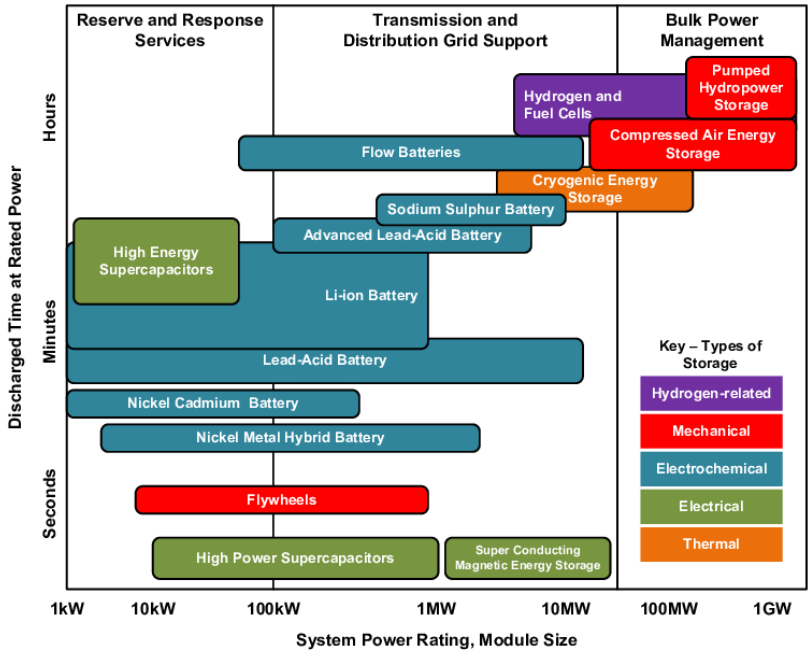

Figure 1. Applicable power ranges and discharge power duration of different energy storage technologies.[1]

I . Introduction

Unlike “primary” lithium batteries, the “secondary” lithium-ion batteries (LIBs) are rechargeable. LIBs were proposed by a British chemist M Stanley Whittingham in the 1970s [3] and were introduced to the market by Sony for the first time in 1991 [4]. Li-ion batteries have widely been used in portable electronic devices and power tools because of its high energy density and efficiency among practical secondary batteries. By 2011, Li-ion batteries accounted for 66% of all portable secondary battery sales in Japan [5]. The next targets of LIBs are considered to be automotive applications and extremely large energy storage systems. Lithium-ion battery technology is based on the shuffling of lithium ion between positive and negative electrode during the charge and discharge process, and therefore the lithium ion battery, is also known as the 'rocking-chair batteries. The work mechanism of Li-ion battery was shown in figure 2, for instance $LiCoO_2$ and graphite were used as cathode and anode electrode. When the battery is fully charged, the anode is maximally full of lithium, with one lithium atom attached to six carbon atoms [6]. During the discharge process, lithium ion was moving from anode (positively charged electrode) to cathode (negatively charged electrode). The reacting compound at the anode and cathode determine the capacity and voltage of a battery. The most commonly used electrode material for Li-ion battery is lithium cobalt oxide ($LiCoO_2$), which offers high energy density but present safety risks, especially when damaged, also high cost and limited for the resources. Lithium iron phosphate ($LiFePO_4$), lithium ion manganese oxide battery ($LiMn_2O_4$, $LiMnO_3$, or LMO), and lithium nickel manganese cobalt oxide offer lower energy density but longer lives and less likelihood of fire or explosion [7,8]. Meanwhile, another concerning issue is lithium resources, because the lithium resources are limited, and the cost of lithium-based raw materials has roughly doubled from the first practical application in 1991 to now, and it will increase more when the demand for lithium increases as the large-scale commercialization of LIBs [9,10].

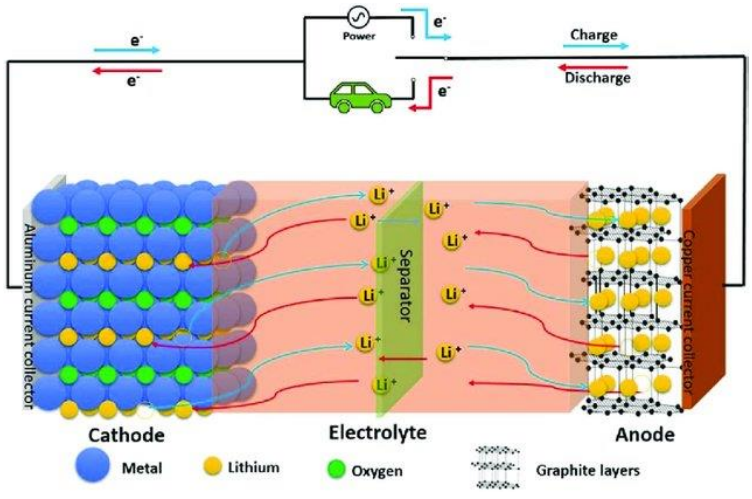

Figure 2. Schematic of the working mechanism of a lithium-ion battery. [6]

For stationary applications of the cells, the main parameters which must be considered are price ($ W h^{-1} kg^{-1}), lifetime (years, cycle number), power density (W kg^{-1}), safety. This requires raw materials with an abundant availability (low price). For this reason, the greater abundance and accessibility of alkali metal (Na^+, K^+) and alkaline earth metal (Mg^{2+}) compared with lithium promote investigation of Na-ion, K-ion and Mg-ion battery. Meanwhile, use of the Li-metal anode induces severe safety issues associated with growth of Li dendrite during the cycling of battery. So, some dendrite-free metal (K, Mg etc.) were ideal anode material. Meanwhile all alkali-metal ions (Li^+/ Na^+/ K^+), they have a similar tendency of losing electrons, as shown in the table 1, the potential of Na^+/Na is -2.71V (0.3V higher than Li^+/Li -3.04V), and the difference between K^+ /K (-2.93V) and Li^+/Li is only 0.11V [11-12]. So, it's shortcut to shift research focus to Non-Li ion systems, because most of the research experiences and well-developed electrodes of LIBs can be directly transplanted to the Non-Li-Ion batteries.

1.1.1 Sodium-ion batteries (SIBs)

SIBs were initially studied along with LIBs in the late 1970s and through the 1980s [13]. Owing to their relatively low cost and the higher abundance in nature of sodium (the fourth most abundant element on Earth) from the alkali metal family, SIBs are regarded as cost-effective choices particularly when large-scale applications are needed. With the success commercialization of Li-ion batteries in 1989, almost all researches in the world were focused on lithium materials and related systems.

Since 2008 the number of published researches on Na battery materials increased very rapidly as many new labs join in this topic [14], this change because of: i) the difficulty to find new materials to the Lithium battery system. During the past years, several materials with potentially interesting insertion and release capability for Na were tested. All that research mainly focused on working to improve the known material for application and to understand the fundamental mechanisms involved in electrochemical process; ii) Concerning the distribution of lithium in the earth crust and the cost of feedstock, researchers are trying to explore new fields with elements other than lithium. Meanwhile this was also an easy path because most of the structure of lithium and sodium materials is very similar, because SIBs and LIBs use a similar intercalation chemistry, the synthesis routes are well described [15].

Various cathode materials for SIBs have been reported, for instance, layered oxides (like Na_xMO_2, M=Co, V, Mo) [16-18], polyanions oxide (like $NaM_2(PO_4)_3$, M= Ti, V) [19] and Prussian blue analogues and polymers [20-22]. However, the research for an anode with appropriate Na voltage

storage, a large reversible capacity and high structural stability remains an obstacle to development of SIBs. One notable feature of a SIB is that the use of graphite, which is common in LIBs, but is unfavorable owing to the difficulties associated with the insertion of Na^+ into the graphite interlayers. Non-graphitic anodes, which consist largely of various carbonaceous materials, such as carbon black and pitch-based carbon allow insertion of sodium ions. Hard carbon, which is synthesized at high temperature from carbon-based precursors, have been comprehensively characterized and tested in Na cells. These non-graphitic carbonaceous materials are considered to be the "first-generation" anode of choice for SIBs systems [23]. SIBs cannot be fabricated with sodium metal due to dendrite formation, high reactivity, and an unstable passivation layer in most organic electrolyte at room temperature.

1.1.2 Potassium-ion batteries (PIBs)

Potassium has an abundance similar to sodium in the earth, but the development of a K-ion battery is lacking behind because of the higher mass (39 g/mol) and large ionic size of K^+ (1.38 Å) than that of Li^+ (0.76 Å) and Na^+ (1.02Å), which makes it difficult to identify a high-voltage and high-capacity intercalation cathode host [24]. But potassium has a low reduction potential than sodium, which allows KIBs to operate at higher potentials, and this potential difference could engender KIBs with higher energy densities than SIBs. In addition, potassium is the seventh most abundant element in the earth crust, the cost of potassium carbonate is much lower than that of lithium carbonate. Another stimulus for potassium battery is the recent development of k^+ anode material. Typical graphitic carbons used in li-ion batteries do not intercalate Na^+ ions but work for with K^+ [25-26]. Hard carbons work for both, but they show more promising performance as K^+ anode [27]. The dendrite-free, liquid K-Na alloy anode acts as a potassium anode. All the above observations tell us to shift attention to potassium batteries.

K-ion batteries have been studied since 2004, Ali Eftekhari [28] designed a potassium secondary cell by using potassium anode and Prussian blue (PB)-based cathode, tested in nonaqueous electrolyte 1M KBF_4 in 3:7 EC/EMC, and this battery shown an excellent cyclability for more than 500 reversible cycles. After that Cui's group synthesized Nickel hexacynoferrate and copper hexacyanoferrate as cathode material and were used in aqueous sodium and potassium ion batteries (1M $NaNO_3$ and 1M KNO_3) shown excellent cyclability, even at high C-rate [29,30]. In addition to hexacyanometallates, layered oxide $AxMO_2$ (A=Li, Na, K, etc.; M=Fe, Mn, Ni, Co, etc.) [31-33] and polyanionic compound ($KFeSO_4F$, $K_3V_2(PO_4)_3$, $KVPO_4F$) are also widely used as cathode material [34-35]. For anode material, graphite is the state-of-the-art anode material in LIBs and also a feasible negative electrode material in PIBs, in contrast to SIBs where it shows only slow performance.

Except graphite [36], graphitizable (soft) carbon and non-graphitizable (hard) carbon [37, 38], as well as other carbon materials like graphene [39], nitrogen-doped graphene [40] and activated carbon [41] were used as anode in non-aqueous PIBs.

1.1.3 Magnesium-ion batteries (MIBs)

Rechargeable Mg batteries have received intensive attention as affordable rechargeable batteries with high electromotive force, high energy density, and high safety. Mg possesses two valence electrons and has the lowest standard electrode potential (ca. -2.36 V vs. SHE) among the air-stable metals. Magnesium batteries theoretically contain almost twice as much energy per volume as lithium-ion batteries (32.731 GJ/m^3 vs. 22.569 GJ/m^3) [42, 43]. There is another advantage that Mg metal can be used as an active material because Mg metal hardly forms dendrites during plating. However, the slow diffusion of Mg ions in solid crystals prevents the realization of active materials for Mg rechargeable batteries at room temperature. Meanwhile a key drawback to using a metallic magnesium anode is the tendency to form a passivating (non-conducting) layer when recharging, which thought to originate from the decomposition of the electrolyte during magnesium ion reduction, and block further charging [44,45].

Electrochemical properties of magnesium in organic electrolyte have been reported in some complex oxides, like MoS_2 [46], TiS_2 [47], $MgMSiO_4$ (M=Mn, Fe and Co) [48-50], RuO_2 [51] and MnO_2 [52] at higher temperatures. However, these compounds were down-size to nanometric scale (e.g. nanosheets, nanotubes, nanoparticles) to enhance the electrochemical activity, which in turn hinders examination of the reaction mechanism. One exception is the Chevrel compounds Mo_6T_8 (T=S and Se), which work at room temperature. However, the working voltage of the Chevrel compound for the cathode is only ca. 1.2 V, which is far below that of Li-ion batteries (3-5 V). Nevertheless, Chevrel compounds have the significant advantage that a relatively large space exists in the crystal structure, which allows for fast Mg ion diffusion [53-54].

In the present report, some materials with framework structures as cathodes for Mg batteries were investigated, which can alleviate the electrostatic constraint between Mg ions and cathode constituents. Specifically, the redox behavior of Prussian blue and Prussian blue analogues in electrolytes containing an Mg salt. In 2013, Mizuno et al. [55] first reported the electrochemical intercalation of Mg^{2+} in CuFe Prussian blue analogue in aqueous electrolyte and shown excellent rate capability, and X-ray absorption near edge structure revealed redox of both Cu and Fe, which has not been observed for the monovalent cation intercalation/ deintercalation. Yagi et al. [56] reported the detailed mechanism of the electrochemical insertion/extraction of Mg^{2+} ions in CuFe

prussian blue analogue and found not only Mg^{2+} ions, but also anions, contribute to charge compensation during charge and discharge in aqueous electrolytes, resulting in redox peak splitting. NiHCF also was been used as electrode material for Mg-ion battery and exhibited high power and cyclability.

Table 1. Potential and atomic/ion radius of alkali/ alkaline-earth metal

Alkali/alkaline-earth metal	Potentia (V vs SHE)	Potential (V vs Li^+/Li)	Atomic radius (Å)	Ionic radius (Å)	Hydrated ion radius (Å)
Li^+/Li	-3.04	0	1.34	0.76	2,37
Na^+/Na	-2.71	0.3	1.54	1.02	1,83
K^+/K	-2.93	0.11	1.96	1.38	1,38
Be^{2+}/Be	-1.85	1.19	1.12	0.27	4,08
Mg^{2+}/Mg	-2.36	0.68	1.45	0.72	3,46
Ca^{2+}/Ca	-2.87	0.17	1.94	1.06	3,09
Sr^{2+}/Sr	-2.89	0.15	2.19	1.18	3,09
Al^{3+}/Al	-1.66	1.38	1,18	0,68	-

In addition to Mg^{2+}, other multivalent ions like Zn^{2+}, Ca^{2+}, Al^{3+} have been widely studied because of their high volumetric capacity (Mg: 3832 mAh/mL, Zn: 5855 mAh/mL, Al: 8045 mAh/mL) [57-59]. The doubly or triply charged ion can accept two/ three electrons for a single ion. For intercalation-type batteries, this means fewer ions would need to diffuse into the lattice for a given capacity, which would result in less several lattice distortion and more stable cells. New energy storage chemistry based on multi-valent ions can theoretically improve the energy density and reduce the cost of battery. However, lack of suitable cathode material with desirable capacity

and long-term stability severely restricts the application of multivalent ion batteries. A key issue with multivalent ion insertion is the ion mobility in host materials, which is highly dependent on the size and charge of guest ions. Therefore, the choice of host materials is limited to a great extent.

Meanwhile, except the difference of potential between lithium ion and other alkali-metal/ alkaline-earth-metal ions, we had to consider the size of different insertion ions, because their ion radicals are show different tendency when they are in dehydrated and hydrated state. For the dehydrated ion radius of alkali-metals, they have the trend of $Li^+ < Na^+ < K^+ < Cs^+$, while for the hydrated ions, they show totally different order: $Li^+ > Na^+ > K^+ > Cs^+$, and the same situation is also found in alkaline-earth-metals [60]. So, when we want to find suitable cathode materials for different battery systems, we had to consider their ionic size. Because the main reaction occurs through intercalation, large channels are essential for accommodating ions into the crystal structure of the cathode material. It's likely that rigid structures are favorable to ensure long-term cyclabilities with high capacities.

1.2 Electrode material

To date, the main design strategies for cathode materials involve transition-metal oxide, transition-metal polyanions and Prussian blue analogues. Here, our job mainly focuses on the Prussian blue and its analogues as both anode and cathode electrode material owing to their inherently open framework structure with large interstitial sites, low cost, and easy accessibility

1.2.1 Prussian blue (PB)

Prussian blue (PB) is a dark blue pigment which was discovered by a Berlin draper in the eighteen centuries [61]. According to its structure we got two well-characterized forms of PB: "soluble" and "insoluble" forms and both show cubic lattice structure with building framework Fe (Ⅱ)-C-N-Fe (Ⅲ) [62]. The "Soluble" form has a regular face-center cubic structure F-43m, where Fe (Ⅱ) and Fe (Ⅲ) are octahedral coordinated to –CN and –NC groups, respectively. "Insoluble" structure has a cubic framework as well (pm-3m), but 1/4 of the Fe $(CN)_6$ sites are vacant, with the empty nitrogen positions filled out by water molecules, instead, which are coordinated to Fe (Ⅲ). Hence, Fe(Ⅲ) atoms are presented in this unit cell with three pseudo-square planar coordinated atoms (FeN_4O_2) and one octahedrally coordinated Fe(Ⅲ) atom (FeN_6), resulting in an average of $FeN_{4.5}O_{1.5}$ [63-64].

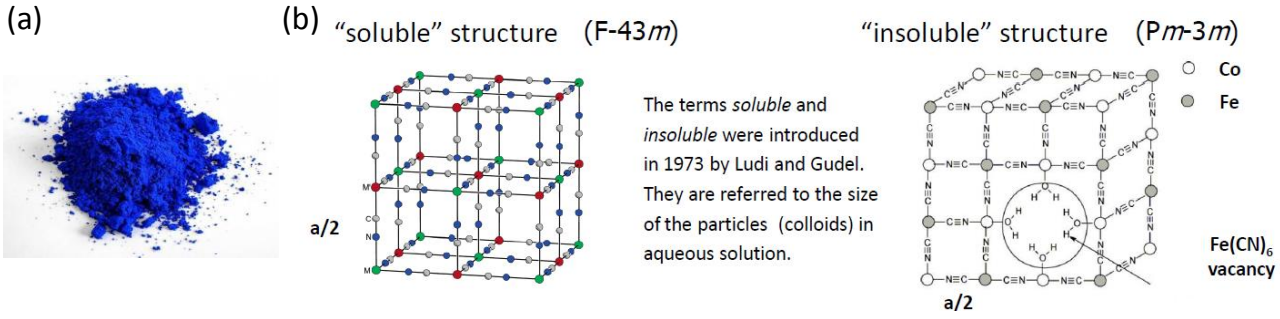

Figure 3. (a) Prussian blue powder; (b) "Soluble" and "insoluble" structure of Prussian blue.

In addition to PB itself, two additional closely related compounds have been found. They are Everitt's salt $K_2Fe^{II}Fe^{II}(CN)_6$, which is colorless, all the iron atoms are ferrous and all cubes contain an alkali atom, and Berlin Green $Fe^{III}Fe^{III}(CN)_6$, the oxidation product of Prussian blue, here all the iron atoms are ferric and there are no alkali atoms present [65], as shown in figure 4.

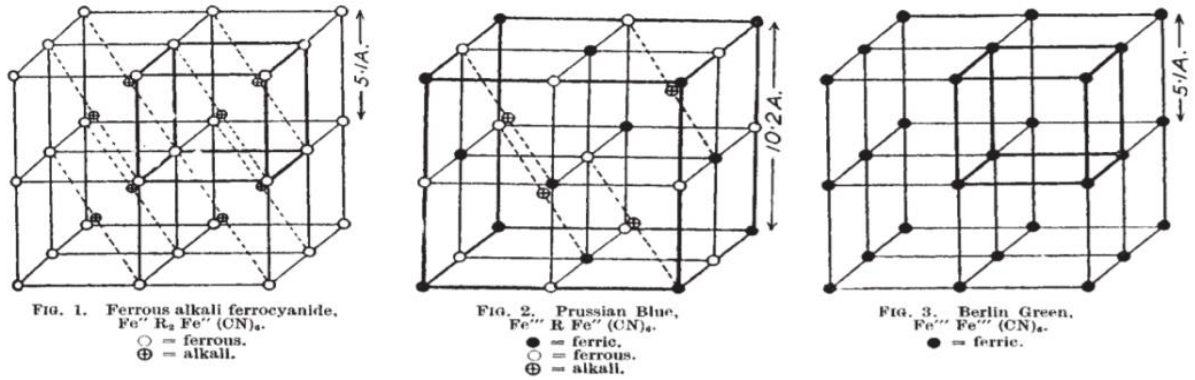

FIG. 1. Ferrous alkali ferrocyanide, $Fe''R_2Fe''(CN)_6$. ○ = ferrous. ⊕ = alkali.

FIG. 2. Prussian Blue, $Fe'''R\,Fe''(CN)_6$. ● = ferric. ○ = ferrous. ⊕ = alkali.

FIG. 3. Berlin Green, $Fe'''Fe'''(CN)_6$. ● = ferric.

(a) (b) (c)

Figure 4. Structure of (a) Ferrous alkali ferrocyanide, (b) Prussian blue and (c) Berlin green [65].

The electrochemical redox behavior Prussian blue was first reported by Neff in 1978 [63], when cyclic voltammetric characteristic of the PB film electrode was tested in the aqueous medium (1M KCl), the electrode changed color rapidly from blue (anodic side) to colorless (cathodic side), when increase potential, the film became green. The same phenomena also been observed in nonaqueous media (KBF_4), as shown in figure 5, cyclic voltammetric behavior is accompanied by two redox couples in accordance with the following reactions:

$$KFe^{III}[Fe^{II}(CN)_6]\text{“PB”} = Fe^{III}[Fe^{III}(CN)_6]\text{“BG”} + K^+ + e^- \quad (1)$$

$$KFe^{III}[Fe^{II}(CN)_6]\text{“PB”} + K^+ + e^- = K_2Fe^{II}[Fe^{II}(CN)_6]\text{“PW”} \quad (2)$$

The reaction (1), which occurs at 0.86V versus SCE (the second pair of peaks), is referred to the oxidation of PB to so-called “Berlin green” (BG) via one-electron transfer oxidizing high-spin iron in PB lattice. And the reaction (2), which occurs at 0.18V versus SCE (the first pair of peaks) is referred to the reduction of PB to so-called “Prussian white” via one-electron transfer oxidizing the low-spin iron system [28].

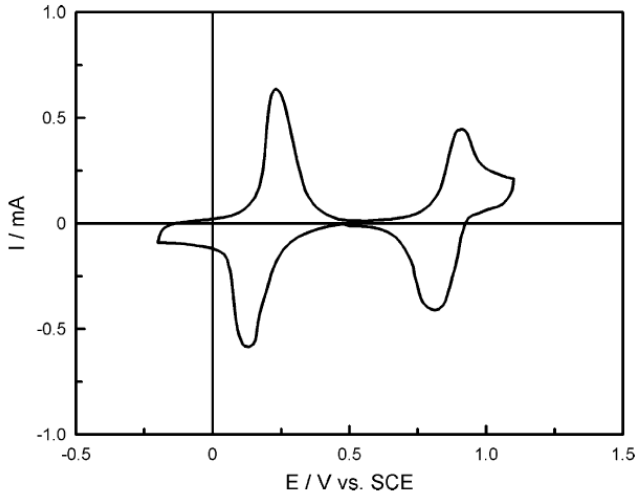

Figure 5. Cyclic voltammetric behavior of the PB film electrode in a nonaqueous electrolyte solution of KBF4. Scan rate 10 mVs^{-1} [28] .

1.2.2 Prussian blue analogues (PBA)

PB allows multiple modifications of its chemical composition without breaking the overall crystal structure of the system. Substitutional and interstitial modifications of PB lead to a series of new compounds generally called Prussian blue analogues (PBAs). When we substitute Fe(III) sites with other metals, such as Zn, Cu, Ni, Mn, Co, V, In etc. [22,29,30,66-67], we get a series of bimetallic cyanide Fe (Ⅱ)-C-N-M with same structure of PB. The crystal structure of PBAs is illustrated in figure 6. The chemical formula of PBA can be expressed as $A_xM'_y[M(CN)_6]\cdot nH_2O$, where A denotes an alkali metal such as Li^+/ Na^+/ K^+, etc.; M' represents transition metal ions such as Fe, Mn, Co, Ni, Mn, Cu, etc.; $0<x<2$; $0<y<1$. The benefits of PBA as ideal insertion/electrode material are illustrated in following:

i) 3D framework and opened ion channel. The same with PB, PBAs also with cubic lattice and M' and M ions are sixfold (octahedral) coordinated to the carbon atom and nitrogen atom of the CN ligands, forming a 3D rigid framework containing open ionic channels and spacious interstitial spaces. Primarily, unlike conventional insertion compounds of transition-metal oxides and phosphates, PB lattices have large interstitial 'A' sites (≈4.6 Å diameter) and spacious channels (3.2 Å diameter in <100> direction), thus giving a high diffusion coefficient of 10^{-9} to 10^{-8} cm^2s^{-1} [68, 69,73] which implies a much higher ionic conduction in the PB lattice than in the conventional insertion cathode of oxide and phosphate.

ii) Two different redox-active centers. PBA compounds contain two different redox-active centers: $M'^{2+/3+}$ and $M^{2+/3+}$ (normally M=$Fe^{2+/3+}$) couples, both of which can undergo a complete electrochemical redox reaction (when M'=Fe, Co, Mn, etc.), contributing a two-electron transfer capacity through reversible insertion/extraction reaction process.

$$A_2\ M'^{II}\ [Fe^{II}\ (CN)_6] \leftrightarrow A\ M'^{III}\ [Fe^{II}\ (CN)_6] + A^+ + e^-$$

$$A\ M'^{III}\ [Fe^{II}\ (CN)_6] \leftrightarrow M'^{III}\ [Fe^{III}\ (CN)_6] + A^+ + e^-$$

iii) Fe site inside the PB compound can be partially or completely substituted by many redox-active transition metals without damaging the crystal structure. This complete composition tenability makes it convenient to tune the electrochemical response of the PB framework. For examples, Na_2FeFe-PB shows charge/discharge plateaus around 3.2V (vs Na/Na^+) [70], whereas Na_2MnFe-PBA and Na_2CoFe-PBA give considerably elevated voltages to 3.6 and 3.8V, respectively [71, 72]. Element substitution can be used to develop high capacity PB cathodes. When the Fe element is completely substituted by Mn, the resulting material Na_2MnMn-PBA material can deliver a greatly enhanced Na-insertion capacity of >200 $mAhg^{-1}$ [73]. Benefiting from the tunable compositions, the electrochemical properties of PBA frameworks can be therefore tailored to fulfill the requirements for battery application.

iiii) PBA lattice is structurally and dimensionally stable during the insertion and extraction process of guest ions. As demonstrated by Cui yi et al., CuHCF can be very well cycled at 17C over 40,000 cycles, and 83% of the original capacity was retained [29].

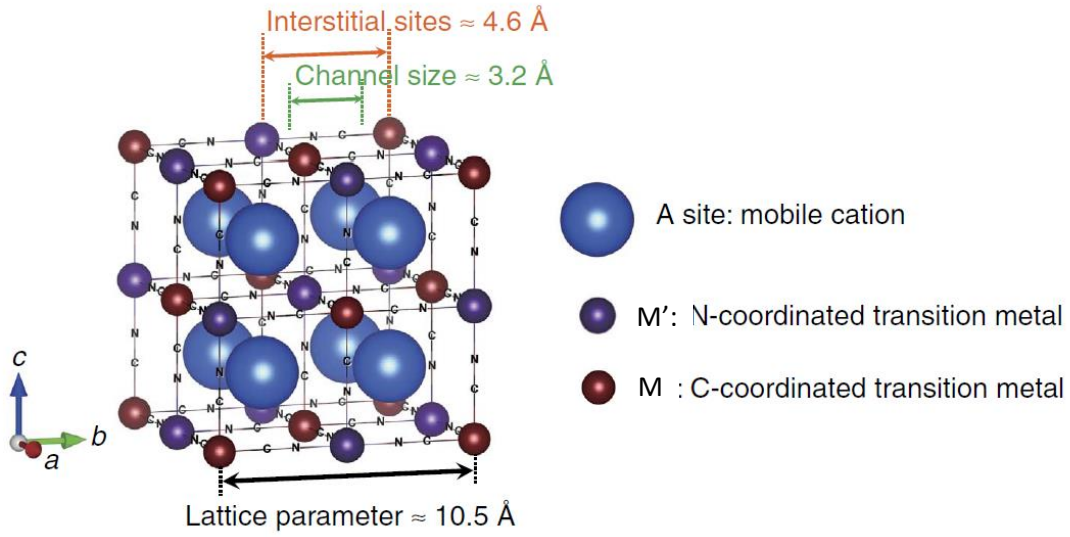

Figure 6 structure of PBA $A_xM'_y[M(CN)_6]\ nH_2O$. Cations A and water are accommodated in A-sites. M' and M are transition metal ions. [73]

Among all the PBAs, copper/ nikel/ manganese/ vanadium/ cobalt/ chromium hexacyanoferrate (HCF) were widely studied in electrochemical reactions And some literatures reported that both metal sites can be electroactive, such as $Fe^{III/II}$ [28], $Cu^{II/I}$ [74], $(V^{IV}O)^{2+}/V^{III}$ [75], $Mn^{III/II}$ [76], but some cases they found only one active species $[Fe^{III/II}(CN)_6]^{3-/4-}$, spread in the battery community [29]. However, the electroactivity of copper in a copper-hexacyanoferrate-based electrode in a battery system was recently unveiled by operando XAS experiment [77]. Based on the job in my lab, we found not only the metal sites, but also the ligands are capable of participating in the redox processes [78]. The complexity of batteries, which consists of different components and various contributions to be overall process, sometimes could be untangled only by using a combined complementary multitechnique approaches.

1.3 Electrochemical techniques

Electrochemical methods are analytical techniques that use a measurement of potential, charge, or current to determine an analyte's concentration or to characterize an analyte's chemical reactivity. Electrochemical processes are commonly used for analytical measurements, and there are a variety of electrochemical methods with different degrees of utility for quantitative and qualitative analysis. Normally, these methods are divided into four major groups: potentiometry, voltammetry, coulometry and conductometry [92]. Here, we only introduce some commonly used electrochemical methods.

1.3.1 Cyclic Voltammetry (CV)

Cyclic voltammetry is a very important and useful electrochemical method that can be used to study the redox behavior of electrode material and probe coupled chemical reaction in order to determine reaction mechanism, the stability of reaction products, the presence of intermediates in redox reactions, electron transfer kinetics etc. [80]. In the CV experiment, the working electrode potential is ramped linearly versus time. Unlike in linear sweep voltammetry, after the set potential is reached, the working electrode's potential is ramped in the opposite direction to return to the initial potential, as shown in figure 7. These cycles of ramp in potential can be repeat many times.

In CV test, the potential is measure between the working electrode and reference electrode, while the current is measured between the working electrode and counter electrode. The current at the working electrode is plotted versus the applied voltage to give the cyclic voltammogram trace, as shown in figure 7. When we apply a reduction potential from V1 to V2, the cathodic current will increase over this time period assuming that there is reducible analyte in the system. At some point after the reduction potential of the analyte is reached, the cathodic current will decrease as the concentration of reducible analyte is depleted. When the redox couple is reversible then during reverse scan (from V2 to V1), the reduced analyte will start to re-oxidized, giving rise to a current of reverse polarity (anodic current) to before. The more reversible the redox couple is, the more similar the oxidation peak will be in shape to the reduction peak, and oxidation and reduction peaks are separated of about 60mV for a monoelectronic process. The ratio of the peak currents at the anode (I_{pa}) and the cathode (I_{pc}) is 1 for a reversible system. The peak currents are proportional to the square root of the scan rate, as expressed in the Randles-Sevcik equation:

$$I_{pa} = 2.69 * 10^5 \mathrm{z}^{\frac{3}{2}} \mathrm{CAD}^{\frac{1}{2}} v^{\frac{1}{2}}$$

Where I_{pa} is the anodic peak current, z is the number of electrons involved in the reaction, C is the bulk concentration, A is the electrode surface area, v is the scan rate, and D is the diffusion coefficient.

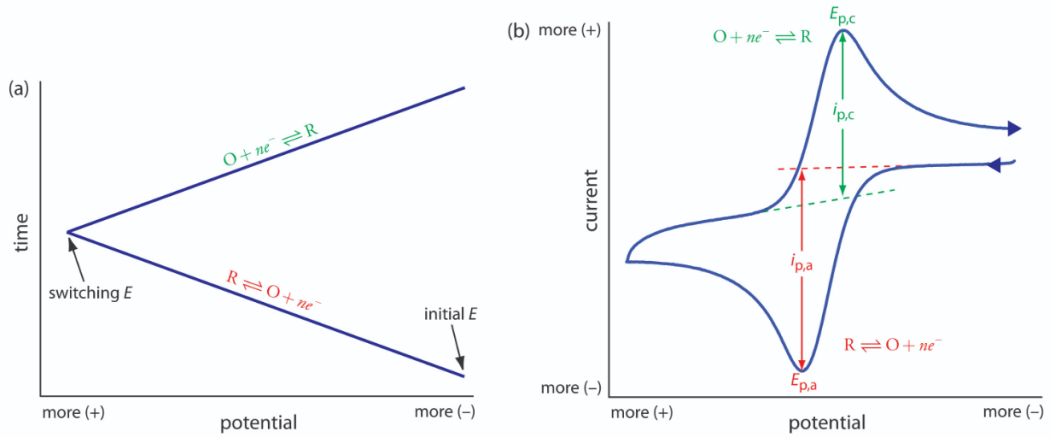

Figure 7. (a) One cycle of the triangular potential-excitation signal showing the initial potential and switching potential; (b) The resulting cyclic voltammogram showing the measurement of the peak currents and peak potentials.

1.3.2 Electrochemical impedance spectroscopy (EIS)

Electrochemical impedance spectroscopy is also called AC impedance or just impedance spectroscopy. It is a method of characterization of the electrochemical system. EIS is a frequency domain measurement made by applying a sinusoidal perturbation, often a voltage, to a system. The impedance at a given frequency is related to processes occurring at time scale of the inverse frequency.

Electrochemical impedance is usually measured by applying an AC potential to an electrochemical cell and then measuring the current through the cell. Assume that we apply a sinusoidal potential excitation. The response to this potential is an AC current signal. This current signal can be analyzed as a sum of sinusoidal functions (a Fourier series). This is done so that the cell's response is pseudo-linear. In a liner (or pseudo-linear) system, the current response to a sinusoidal potential will be a sinusoid at the same frequency but shift in phase (see figure 8) [81].

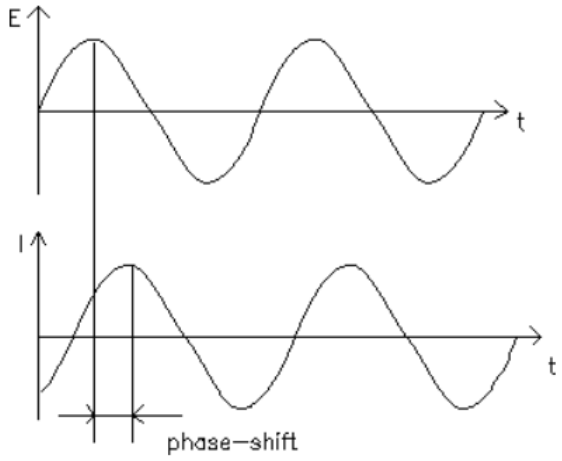

Figure 8. Sinusoidal current response in a linear system

The excitation signal expressed as a function of time, has the form: $E_t=E_0\sin(\omega t)$, where E_t is the potential at time t, E_0 is the amplitude of signal, and ω is the radial frequency. In a linear system, the response signal, I_t is shifted in phase (Φ) and has a different amplitude than I_0.

$$I_t = I_0 \sin(\omega t + \Phi)$$

An expression analogue to Ohm's law allow us to calculate the impedance of system as:

$$Z = \frac{E}{I} = \frac{E_0 \sin(\omega t)}{I_0 \sin(\omega t + \Phi)} = Z_0 \frac{\sin(\omega t)}{\sin(\omega t + \Phi)}$$

The impedance is therefore expressed in term of a magnitude Z_0, and a phase shift Φ.

With Eulers relationship: $\exp(j\phi) = \cos\phi + j\sin\phi$

Where ϕ is real number and j is imaginary unit.

It is possible to express the impedance as a complex function. The potential is described as,

$E_t=E_0 \exp(j\omega t)$ and current response as, $I_t = I_0 \exp(j\omega t - \Phi)$

The impedance then represented as a complex number:

$$Z(\omega) = \frac{E}{I} = Z_0 \exp(j\Phi) = Z_0(cos\Phi + j\sin\Phi)$$

The EIS data can be presented as Bode plot or a Nyquist plot as show in figure 9.

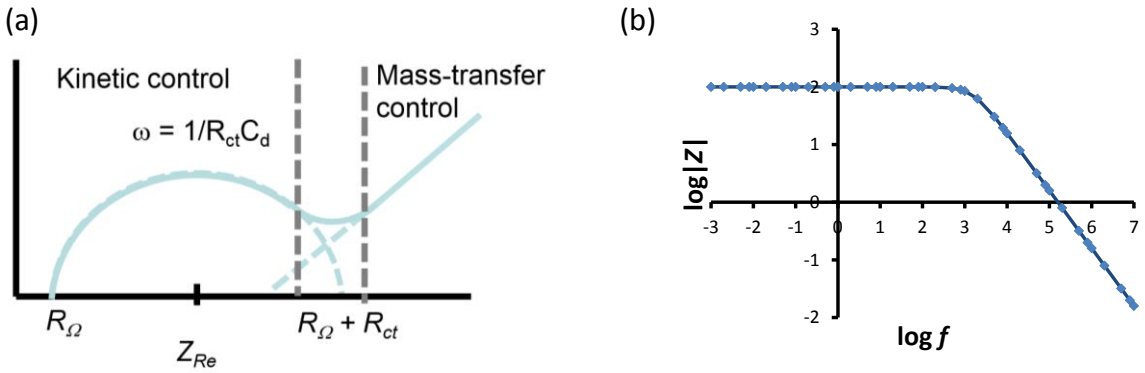

Figure 9. (a) Nyquist plot and (b) Bode plot of impedance spectroscopy.

1.3.3 Galvanostatic charge-discharge technique

Galvanostatic refers to an experiment technique whereby an electrode is maintained at a constant current in an electrolyte. This technique is used to study the performance of the battery over the lifetime of the cycling, corrosion rate and electrochemical reactions. In galvanostatic test, the change is plotted in potential verses time at constant current (figure 10).

During the galvanostatic cycling of batteries, the charge and discharge current are often expressed as a C-rate, calculated from the battery nominal capacity, i.e., the capacity value the battery has when completely charged. The C-rate is a measure of the rate at which a battery is completely charged or discharged, relative to its nominal capacity. For example, a C-rate of 1C means that the current necessary for complete charge and discharge in one hour is applied. In battery research, it's common to use a C-rate of 0.1C, to charge and discharge a battery in ten hours. The current i (A) is calculated multiplying the C-rate by the ratio between the battery nominal Cmax (Ah) and one hour time (h)

$$i\ (A) = \text{c-rate} * \frac{\text{Cmax (Ah)}}{1\ (h)}$$

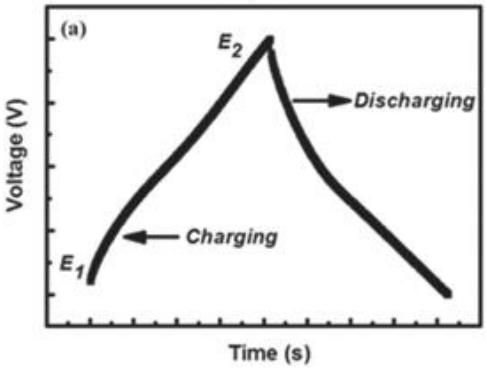

Figure 10. Galvanostatic charge-discharge curve

Normally for the galvanostatic cycling test, we will assemble some coin cells. The commonly used coin cell cases are 2032/2025. Both are 3 V button cell, around 20 mm in diameter, but the 2032 is 3.2 mm thick while the 2025 is 2.5 mm thick. Except the coin cell case, inside the coin cell are stacked layers, as show in figure 11. From the top to bottom, there are spacer (stainless steel Wave-spring/ space Disk), anode, separator, and cathode. After having been stacked, coin cells are closed by means of a mechanical machine.

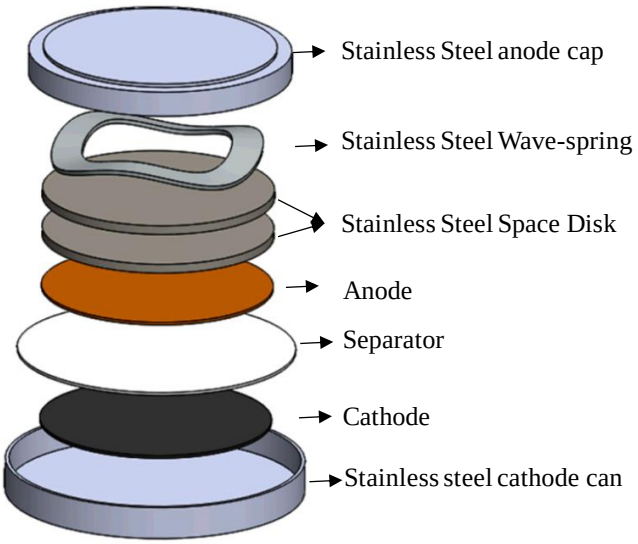

Figure 11. The schematic and assembling of coin cell.

II. Experiment and Characterization

Most of the PBAs are been used as cathode material. However, Ti-based compounds shown different tendencies, and they have been extensively investigated as both cathode (TiS_2, Ni/Mn/Fe/Co-Ti binary/ternary/multinary system) and anode materials ($Li_4Ti_5O_{12}$, $MLi_2Ti_6O_{14}$, TiO_2 etc.) [79]. Because those titanium-based compounds present low-strain and high-stability characteristics as electrode material, they potentially enable low-cost and long-life room-temperature towards large-scale energy storage systems. Meanwhile titanium element plays a critical role in both positive and negative electrode, i.e., supplying the charge transfer and high safety for anode and greatly enhancing the structure and cycling stability for cathode. Based on the bi-functional roles of titanium, a concept of synthesizing titanium hexacyanoferrate and use them as either cathode or anode material or both was proposed. In this work, we synthesized Ti Hexacyanoferrate (TiHCF) by simple precipitation method and tested them as electrode material in both aqueous and organic electrolyte systems.

2.1 Experiment

Titanium hexacyanoferrate (TiHCF) Synthesis and electrode preparation

The synthesis of TiHCF was based on a simple and reproducible method, by mixing 50ml 0.1M tertbutyl titanate ethanol solution with 100ml 0.1M $Na_4Fe(CN)_6$ aqueous solution containing 1.5M HCl under continuous stirring to obtain a precipitate. Because tertbutyl titanate is easily hydrolyzed, it was mixed with ethanol, and dropwise added to $Na_4Fe(CN)_6$ solution, under N_2 atmosphere. After that the suspension was maintained at 60℃ for 4h under N_2 atmosphere. The as-obtained dark-green precipitate was centrifugated and washed with water and acetone for several times, and finally dried in vacuum oven at 70℃ for overnight.

The working electrode was prepared by mixing the active material (75%), carbon black (25%) and PTFE (5%) together and grinding until we get homogenous thin solid slice. We use puncher (with diameter 5mm) to get pellet, then we use aluminum mesh to fix the pellet and use it as work electrode.

Table 2. The mass of pellets we used in different electrolyte

Electrolyte (0.1M)	Formula	Pellete (mg)	AM (mg)
$NaNO_3$	AM: Carbon black: PTFE = 70%: 25%: 5%	1,4	0,98
$Mg(NO_3)_2$		1,2	0,84
KNO_3		1,6	1,12

2.2 Electrochemical tests

First the electrochemical properties of the obtained material were evaluated in three-electrode mode aqueous system, Saturated calomel electrode (SCE) as reference electrode, Platinum wire as counter electrode (figure 12).

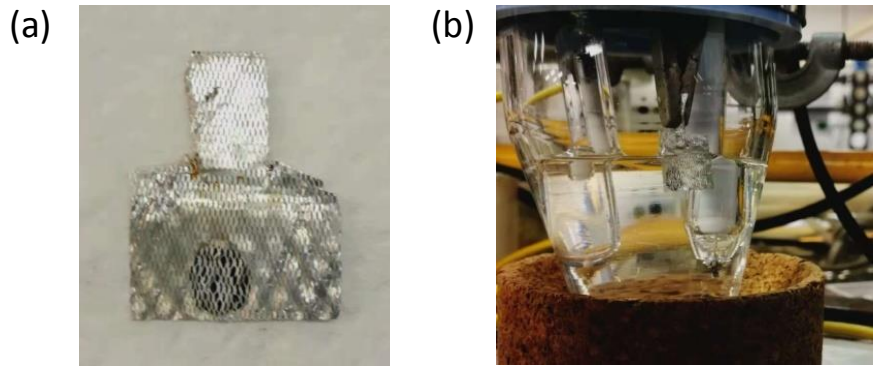

Figure 12. (a) TiHCF electrode fixed by aluminum mesh; (b) Three-electrode test system.

Cyclic voltammetry (CV) was performed by means of CH Instruments Model 660, while a MTI-battery analyzer was employed for galvanostatic cycling with potential limitation (GCPL). For the CV test of coin cells, and short-cutting of reference and counter electrode cables was needed.

For galvanostatic cycling test, we prepared two kinds of coin cells: Li-ion battery and Na-ion battery. A large piece of lithium metal foil was adopted as negative electrode, and for both counter and reference electrode in cycling voltammetry. 1M $LiPF_6$ in an ethylene carbonate: 1 dimethyl carbonate volumetric mixture (EC: DMC) without additives was used as electrolyte for Li-ion battery. And for Na-ion battery, metal sodium was used as negative electrode and $NaPF_6$ was used as electrolyte. Positive electrode, Whatman separator soaked in the electrolyte, and negative electrode were stacked and assembled in a 2036 stainless steel coin cell under inert atmosphere in an Ar-filled glovebox.

The CV test was conducted at the potential range of -1.3~1.3 V vs SCE in aqueous electrolyte at different scan rate (20 mV/s, 10 mV/s, 1 mV/s), starting from OCP conditions with positive polarization.

Galvanostatic cycling with potential limitation (GCPL) was conducted in 2.0-4.3V vs. Li^+/Li potential window at different current densities, by considering 1C rate equals to the current needed to insert one equivalent of Li-ion per equivalent of Fe in one hour, and thus a theoretical specific capacity of 83.6 $mAhg^{-1}$ for the starting material. For Na-ion coin cells we use 2.0-4.2V vs. Na^+/Na as potential range. Cycling started after a rest time (400 seconds) at OCP condition with a positive imposed current.

2.3 Material characterization

Microwave plasma-atomic emission spectrometer (MP-AES) composition analysis was tested by MP-AES 4210 atomic emission spectrometer. During the test, first different concentration (0, 10ppm, 20 ppm, 30 ppm and 40 ppm) standard solution of Fe, Ti and Na was prepared (diluted by 0.5M nitric acid); then the sample was solved in 0.5M nitric acid. Three different analytical lines (wavelengths) were chosen for each element during the test.

Infrared spectrum was tested by Bruker Alpha FT-IR spectrometer in ATR (attenuated total reflectance) mode at spectral range of 4000-400 cm^{-1}.

Powder X-ray diffraction (PXRD) data were recorded on the synthesized powder using a monochromatic X-ray beam with a wavelength of 1 Å at the MCX beamline in ELETTRA synchrotron Trieste, Basovizza (Italy). Data were collected on the sample in a capillary geometry, setting the spinner at 300 rpm. The X-ray diffraction (XRD) pattern was collected consecutively in the range $8^o<2\theta<56^o$, with steps of 0.01 º and an acquisition time of 1s/step. The crystal structure was refined using Fullprof Suite.

Thermogravimetric analysis (TGA) was performed in air from room temperature to 500℃, with a heating rate of 5℃/min, and rapid cooling.

X-ray absorption spectroscopy (XAS) experiments were conducted at Elettra Sincrotrone Trieste, Basovizza (Italy), at XAFS beamline. The storage ring was operated at 2.0GeV in top-up mode with a typical current 300 mA. Data were recorded at Ti K-edge in transmission mode using ionization chambers filled with a mixture of Ar, N_2, and He to have 10, 70, and 95% of absorption in the I_0, I_1 and I_2 chambers, respectively. An internal reference of titanium was used for energy calibration in each scan. This allowed a continuous monitoring of the energy during consecutive

scans. The white beam was monochromized using a fixed exit monochromator equipped with a pair of Si (111) crystals. Spectra were collected with a constant k-step of 0.3 nm^{-1} with 3s per point acquisition time from 4880 to 5600 eV (Ti K-edge). XAS spectra were calibrated using the Athena program.

III. Result and discussion

The stoichiometry of the resulting TiHCF be written as $Na_{0,86}$ $Ti_{0,73}[Fe(CN)_6]\cdot$ $3H_2O$ (M=320,58 g/mol) after MP-AES composition analysis, which provided a Na/Ti/Fe ratio of 0.86/0.73/1. According to the formula weight, we calculated the theoretical capacity of active material is 83.6 mAh/g when considering 1 mol Na^+ participating reaction, calculated by equation (1).

$$\text{Theoretical capacity} = \frac{F(C/mol)}{M(g/mol)*3.6} mAh/g = \frac{96485}{320.58*3.6} = 83.6 mAh/g \ldots\ldots\ldots \text{ equation (1)}$$

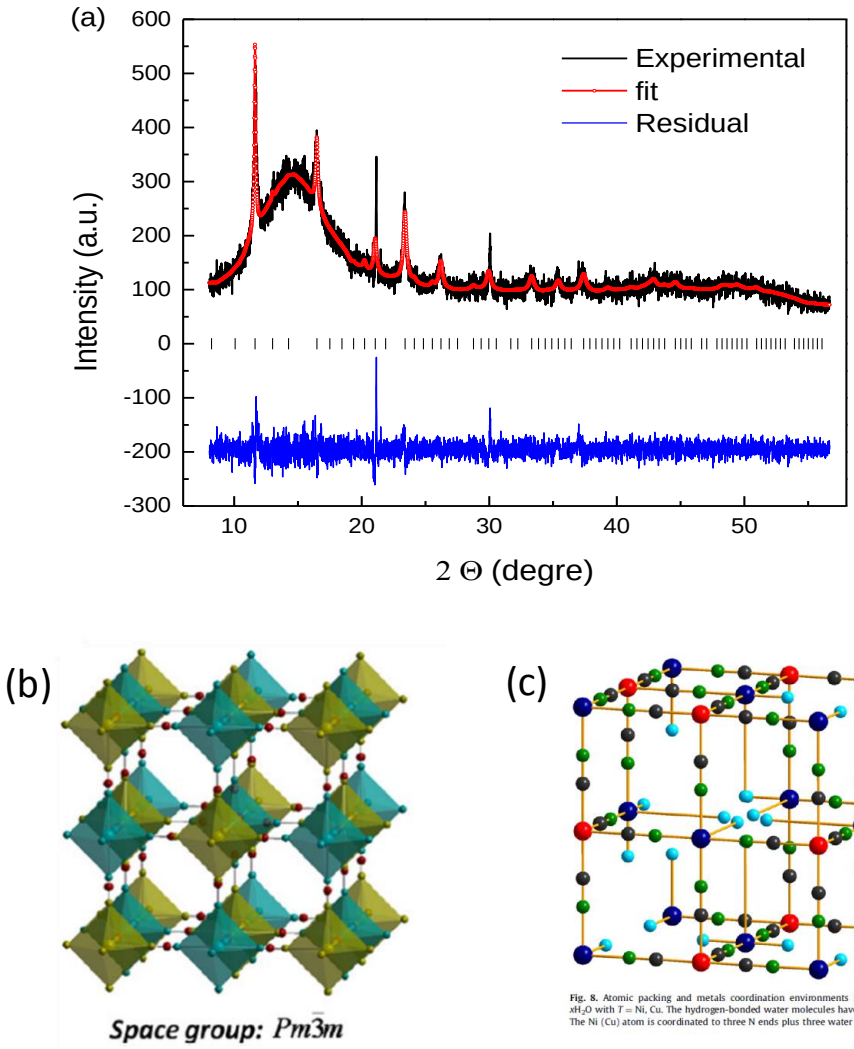

Figure 13. (a) XRD spectrum of TiHCF; (b) Space group Pm3̄m [82] and (c) Atomic packing and metals coordination environments in T_2 [Fe $(CN)_6$] · xH_2O. The hydrogen-bonded waters have been omitted. The T atom is coordinated to three N ends plus three water molucules [83].

Powder X-ray diffraction (XRD) profile of the as-synthesized sample and its profile matching refinement shown in figure 13. XRD test was performed in the range of 8º<2θ<56º. The profiles were refined with 'Tompson-Cox-Hastings pseudo-Voight* Axial divergence asymmetry' peak shape using Fullprof Suite software. The refinement the powder pattern led to a cubic structure (space group: p m-3 m) characterized by the lattice parameter a=9.8625Å. As shown in figure 13 (b), Pm-3m type PBAs, the octahedra of the divalent metal ion is formed by 3N ends of CN group and 3O atoms from water molecules. The occupation of the free volume within the framework is completed by water molecules hydrogen bonded to the coordinated ones. The cell volume per formula unit is 479.66 $Å^3$, very close to the value reported 508.76 $Å^3$ for $Ni_2[Fe(CN)_6] \cdot xH_2O$ and 494.45 $Å^3$ for $Cu_2[Fe(CN)_6] \cdot xH_2O$ [83]. The large value for the cell volume per formula unit indicates that their structure is relatively open, where a large free volume is available.

Table 3. Space group and cell parameters of TiHCF.

Space group	p m -3 m					
Cell parameters	a	b	c	α	β	γ
	9.8625 Å	9.8625 Å	9.8625 Å	90.0000	90.0000	90.0000

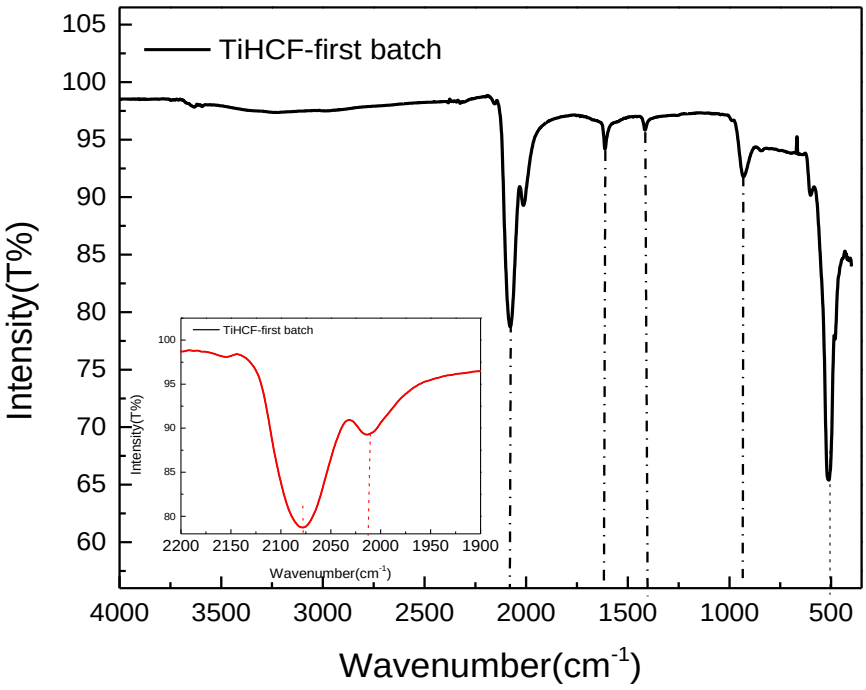

Figure 14. FTIR spectrum of TiHCF

Infrared spectroscopy of TiHCF was shown in figure 14, a broad peak occurs around 3500~3000 cm^{-1}, this can be attributed to the stretching mode of -O-H group, because of the coordinated water inside the structure. Meanwhile, the peak at 1610 cm^{-1} is related to the absorbed water due to the bending mode of -O-H group. A distinguishable peak and a small peak appear at around 2075 cm^{-1} and 2010 cm^{-1} which is the characteristic peak of -C≡N group. As the cyanide bridge is extremely sensitive to its environment, including the oxidation state and the spin state of the metal cations involved, so the wavenumber of -C≡N group can be used to characterize the state of PBA. Mario Berrettoni et al reported the IR spectra of CoHCF, three bands around 2085, 2120, and 2158 cm^{-1} were observed, and they attribute the band at 2158 cm^{-1} to the CN stretching in the chain Fe^{III}-CN-Co^{II}, the band at 2120 cm^{-1} to the chain Fe^{II}-CN-Co^{III}, and the band at 2085 cm^{-1} to the chain Fe^{II}-CN-Co^{II} [84]. In this case, the vibrational band occurs at 2075cm^{-1} maybe associated to Ti^{III}-N≡C-Fe^{II}; the small peak located at 2010 cm^{-1} maybe due to Ti^{II}-N≡C-Fe^{III}, surface non-bridging cyanides, or Ti^{II}-N≡C-Fe^{II}. If we want to confirm that we have the Ti-N-C-Fe chain, then we wish to find the peaks related to Ti-N and Fe-C bond. According to the report, Metal-N stretching frequency are at low frequency, for example Ti-N stretching frequency appears at 390~350cm^{-1} in the titaniurn halide -diamine complexes and 365~330cm^{-1} in the similar bromide complex. But also, there is a report try to assign of 540 cm^{-1} for Ti-N the stretching frequency [85]. In the spectrum of TiHCF, we had a band around 500 cm^{-1}, so we postulate that it may arise from the stretching of Ti-N band in the chain of Ti-N-C-Fe.

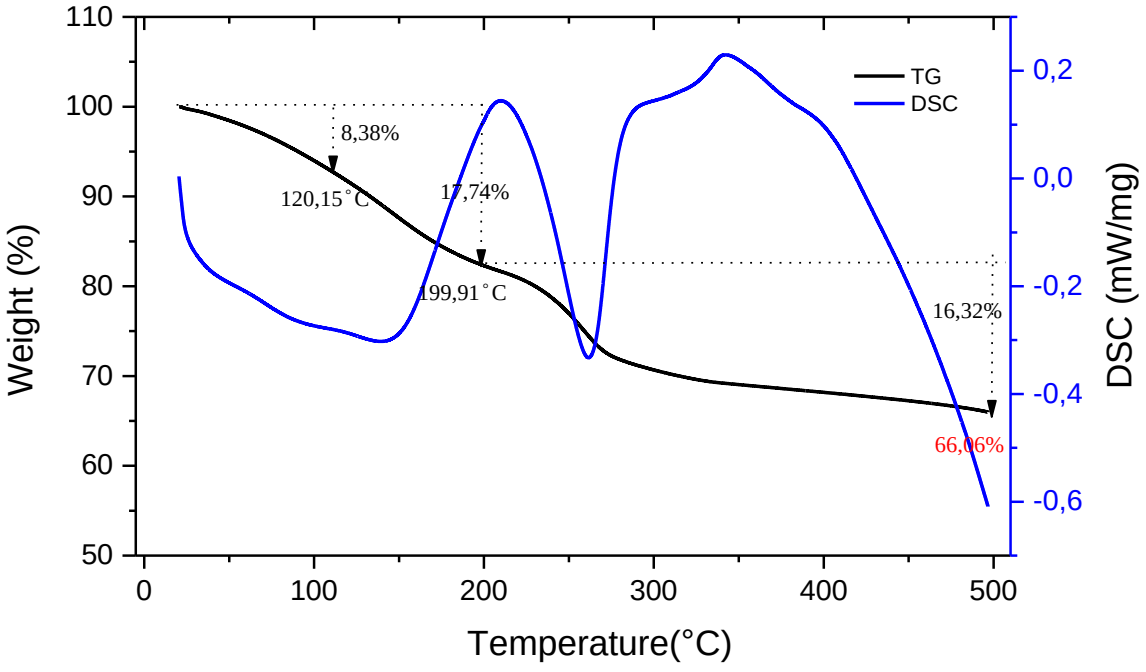

Figure 15. TGA curve of TiHCF.

Thermogravimetric analysis (TGA) of prepared sample shows two distinct weight-loss events, as show in figure 15. Normally the weight-loss below 120℃ corresponding to the loss of adsorbed water, the weight-loss between 120~200℃ can be assigned to the elimination of interstitial water, and then the decrease above 200℃ indicates the decomposition of the framework [2]. In our sample, the total water content is about 17.7%, with around 8.4% adsorbed water and 9.4% interstitial water. When temperature increased to 500℃, it shows another 16.3% weight loss, with 66.1% residues. The calculation of chemical formula of TiHCF was calculated based on 17.7% water content.

The material has been further investigated by using the elemental sensitivity of the x-ray absorption spectroscopy probe for the atomic specie, and therefore the Ti K-edge has been recorded and analyzed. The XAS spectrum is typically divided into two regions, one the X-ray absorption near-edge structure (XANES) where the photoelectron has a low energy; the other called Extended X-ray absorption fine structure (EXAFS) which is characterized by a higher energy of the photoelectron.

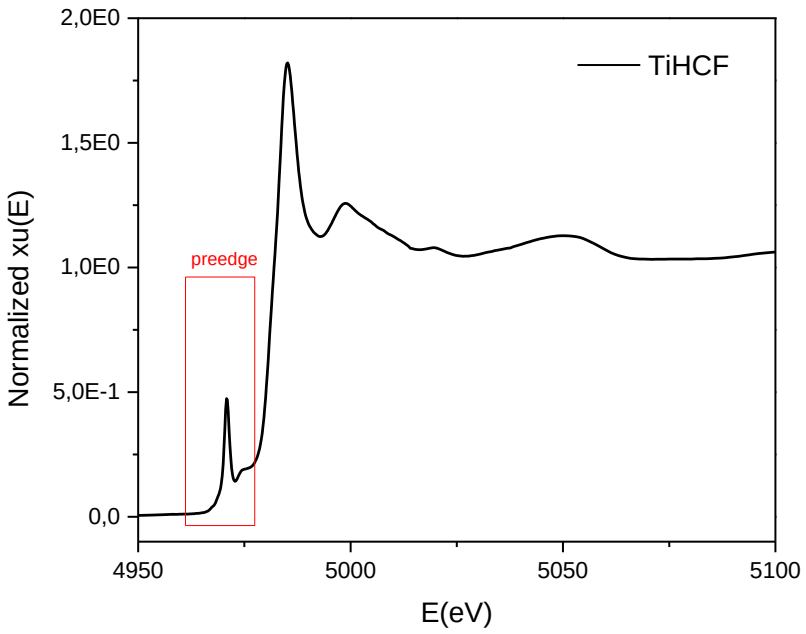

Figure 16. XANES spectrum of Ti K-edge.

The XANES of an X-ray absorption spectrum can be conveniently divided into two regions. The first region, herein called the pre-edge, is the low energy region between the absorption threshold and the absorption jump, while the post-edge region extends to about 50 eV past the threshold. The pre-edge region arises from transitions of electrons to bound excited electronic states, but this electronic excitation is strongly modulated by the surrounding atoms in the short and

medium range (<100 absorption atoms) environment. The pre-edge region therefore contains much potentially useful structure and electronic information, like (i) coordination number, based on the plot of peak energy versus height; (ii) estimate of distortion, using the intensity ratio between pre-edge peaks; and (iii) the bond interaction strength from the rise and fall in peak intensity in the whole pre-edge region [86]. But rigorous theoretical framework is needed to help extract this information. There are two most popular approaches to the interpretation of XANES are through multiple scattering and band structure calculations, which are different ways of calculating the same unoccupied density of state.

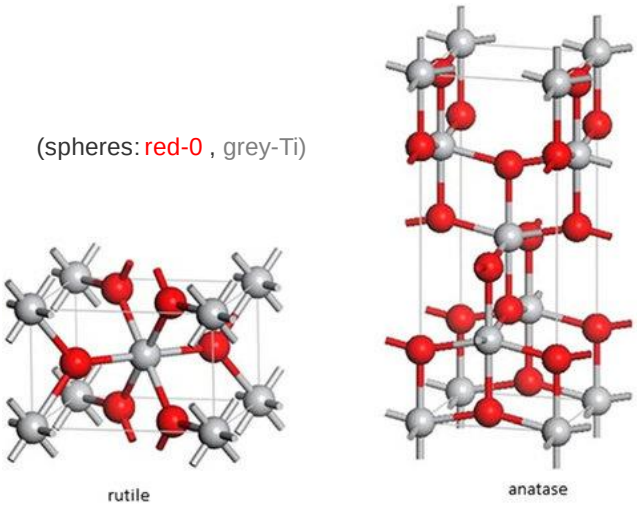

Figure 17. Crystal structure of Titanium dioxide phase of Rutile and Anatase.

Titanium dioxide has two phases: rutile and anatase. Both rutile and anatase are tetragonal, rutile containing six atoms per unit cell and anatase twelve. In both structures, each titanium atom is coordinated to six oxygen atoms and each oxygen atom is coordinated to three titanium atoms. In each case the coordinated oxygen octahedron around the titanium atom is slightly distorted, two Ti-O distances being slightly greater (less than 0.1 Å) than the other four and some of or all the O-Ti-O bond angels deviating from 90^0. This lowers the local point-group symmetry around the titanium atom from O_h to D_{2h} and D_{2h} in rutile and anatase, respectively [91]. The essential difference between rutile and anatase lies in the secondary coordination and in the way that the Ti O_h octahedral are joined together by sharing edges and corners. In rutile, two edges are shared and in anatase four.

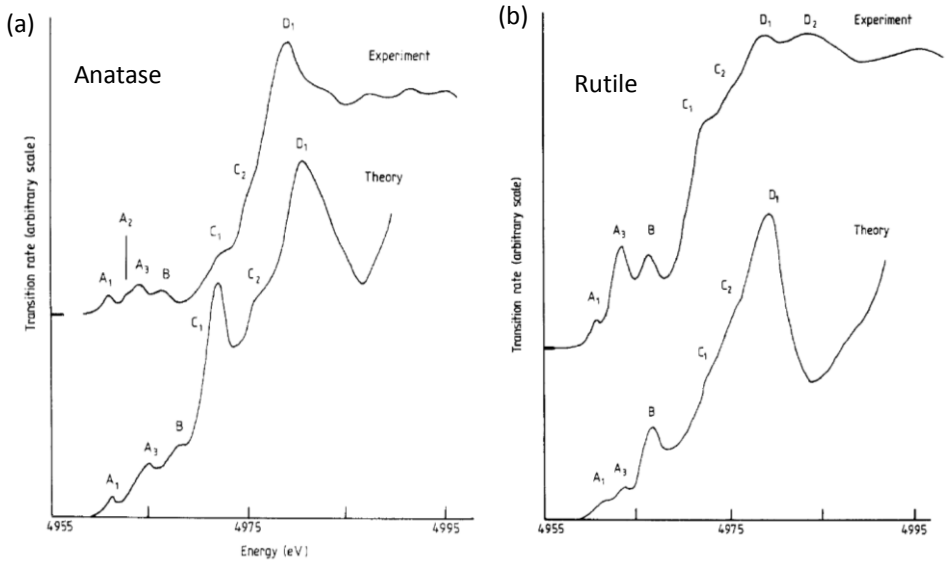

Figure 18. XAS Ti K-edge of Anatase and Rutile from reference [91].

X-ray absorption spectroscopy of the anatase and rutile polymorph of TiO_2 found that at least three pre-edge features can be observed and labeled A1, A3 and B, as shown in figure 18. The feature labeled A2 is sometimes observed as a weak shoulder on the low energy side of the A3 peak in anatase phase and requires good energy resolution to be observed. Despite the similarity between the crystallographic and electronic structure of anatase and rutile, the A2 peak does not appear to be present in the XANES of rutile phase. The pre-edge structures at transition-metal K-edges were related to empty *3d* orbitals, and here there is a general consensus in assigning peaks A3 and B to quadrupolar transition to t_{2g} and e_g orbitals. The XANES results suggest that a significant *3d-4p* orbital mixing occurs in rutile and anatase, forming t_{2g} and e_g bands which do not possess solely *d* symmetry. The presence of three pre-edge features at the Ti K-edge (A1, A3 and B) is accompanied by an increase in distortion at the titanium site.

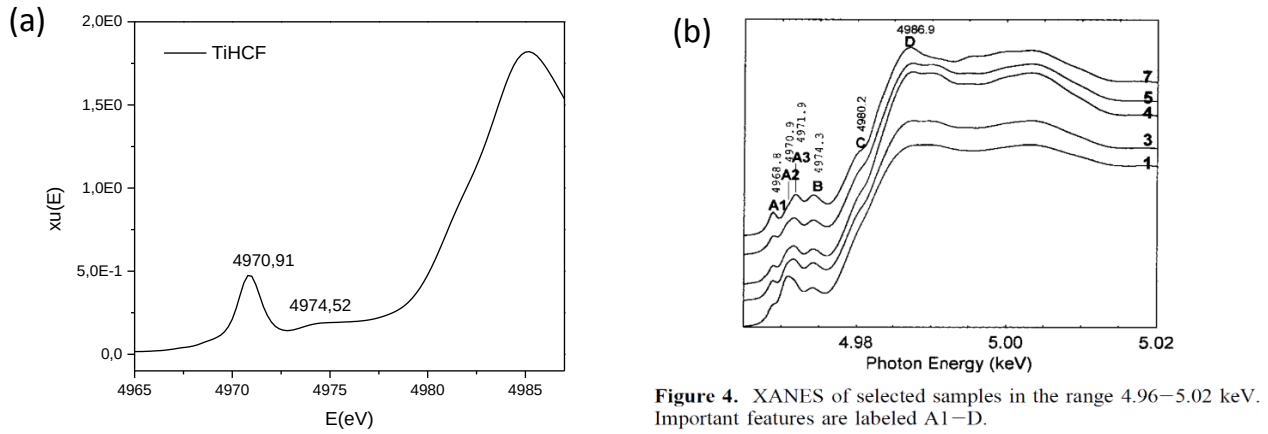

Figure 4. XANES of selected samples in the range 4.96−5.02 keV. Important features are labeled A1−D.

Figure 19. (a) Peak analysis of pre-edge features of Ti K-edge XANES spectrum of TiHCF; (b) XANES spectrum of anatase from reference [86].

In our case (figure 19 a), we found an appreciable peak at around 4970.9 eV followed by a weak one at 4974.52 eV in the pre-edge portion of the TiHCF XAS spectrum. Here the Ti atoms have the same local coordination environment respect to TiO_2, because both of them are octahedral coordinated, oxygen for TiO_2 and here nitrogen for TiHCF. According to another report about Ti K-edge X-ray absorption spectroscopy of the anatase polymorph [86], they specified three pre-edge features and labeled A1 (4968.8 eV), A3 (4971.9 eV) and B (4974.3 eV). Even though there is still controversial about the attribution of pre-edge peaks, there is general agreement that A3 (or all A series transition, less unanimity) and B are due to dipole forbidden transitions of the core electron to *3d-4p* hybridized states. Here, we cannot specify the peaks according to their energy position due to different calibration method or reference samples used, but the presence of pre-edge peaks indicate than there is distortion for the configuration of Ti site, and the two peaks may also attribute to the transition to Ti *3d-4p* hybridized states. Eventually, we see local distortion of Ti octahedral sites.

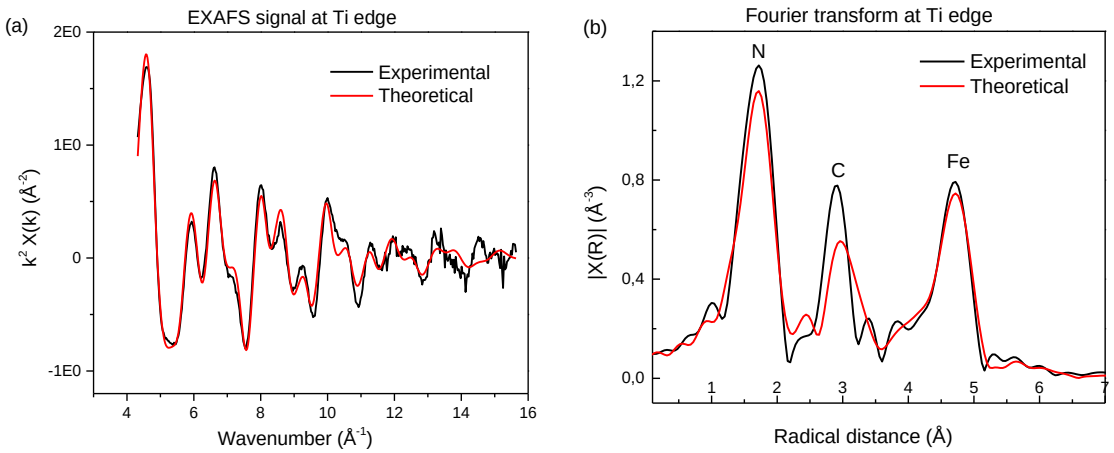

Figure 20. (a) EXAFS of Ti k-edges; (b) Fitting on k^2-extracted EXAFS signal and (c) Corresponding Fourier transform (FT).

Additional structural information can be obtained by looking at the extended portion of the x-ray absorption spectrum (EXAFS). EXAFS is an interference effect that depends on the wave nature of the electrons. It is therefore convenient to think of EXAFS in term of the photoelectron wavenumber k, rather than X-ray energy, according to equation (2), we transfer x (E) signal to x (k). Meanwhile, x(k) signal is weighted by k^2 or k^3 to amplify the oscillation at high k, and Fourier transformation was used to separate the sinusoidal waves from one another, as shown in Figure 20. Figure 20 (a) displays the EXAFS signal fitting at the Ti K-edge for TiHCF, and the theoretical curve displays a better agreement with the experimental one. The structure nature of the sample checked by the magnitude Fourier transform EXAFS of TiHCF shows the existence of three shells of back-scattering atoms around the center Ti. According to the structure of TiHCF, the position of first peak attribute to Ti-N bond (≈1.7 Å), and the second and third peaks can attribute to the shell of Carbon (≈2.9 Å) and Iron (≈4.7 Å).

$$k = \frac{2\pi}{\lambda} = \sqrt{\frac{8\pi^2 m_e (E - E_0)}{h}} \qquad \text{……Equation (2)}$$

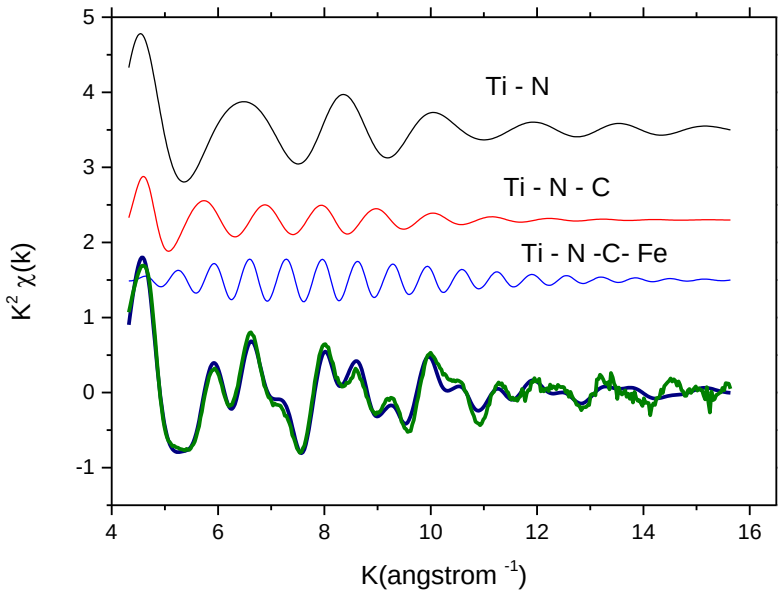

Figure 21. Details of the EXAFS analysis of the Ti K-edge of TiHCF. The figure shows the individual EXAFS contributions, in terms of two-body, three-body, and four-body signals, to the total theoretical signal. The comparison of the total theoretical signal (…) with the experimental one (-) is also reported at the bottom.

Figure 21 reports the details of the EXAFS analysis, taken at the Ti K-edge, in terms of single contributions to the theoretical signals, and the comparison of the total theoretical signal with the experimental, one again demonstrating the reliability of this data analysis. In particular, the signals are due to the different atomic shells above mentioned, the Ti-N first shell, the Ti - - C second shell, and the Ti - - Fe third shell. All the atomic contributions herein reported are significant in the determination of the experimental signal and particular emphasis should be given to the four-body contribution (third shell) due to the other metal, i.e.: Fe atom (by the Ti-N-C-Fe linear chain) is of fundamental importance since it modulates the total EXAFS signal. The best fit has been obtained with E value of 4973.6(6) eV, which is displaced by several eV in respect to the edge inflection point. The value of S_0^2 was found to be 0.65(5). The atomic distances related to the Fe-C-N-Ti linear chain, i.e., the Fe-C, C≡N, and Ti-N distances, have been found to be 1.87(2), 1.18(2) and 2.079(5) respectively, in good agreement to those of similar metal hexacyanoferrate material [93].

IV. Electrochemical applications

Electrochemical measurement of as-prepared sample was conducted by Cyclic voltammetry, galvanostatic charge-discharge and cyclability test. For cyclic voltammetry test, it was performed on the active material with a set of different electrolytes and scan rate by using three electrode system. These electrolytes varied from monovalent cation ions to multivalent cation ions in aqueous electrolyte system, and Li-ion and Na-ion batteries were also tested in organic electrolyte system. Galvanostatic cycling was conducted by using a coin cell, and the material has been tested as positive electrode in organic electrolyte. During the test, there are a set of variables that had to be optimized, such as mass loading, potential window and the scan rate etc. Based on the before research job of my lab on the electrolyte concentration, we choose 0.1M for all the electrolyte that we used here. When not specified, potentials are referred to the Saturated Calomel Electrode (SCE).

4.1 Aqueous electrolyte system

In general, the requirements for an ideal electrolyte are as follows: (1) wide potential window; (2) high ionic conductivity; (3) high chemical and electrochemical stability; (4) high chemical and electrochemical inertness to ES components (e.g., electrode, current collectors and packaging); (5) wide operating temperature range; (6) well-matched with the electrolyte material; (7) low volatility and flammability; (8) environmentally friendly; and (9) low cost. Actually, it is very difficult for an electrolyte to meet all these requirements, and each electrolyte has its own advantages and shortcomings.

The Electrochemistry performance of the as-prepared sample was first investigated in aqueous electrolyte (0.1M $NaNO_3$ / kNO_3 / $MgNO_3$ solution). Compared to organic system electrolyte, the aqueous system batteries show several benefits: (i) Safety. Aqueous system batteries avoid the using of volatile, flammable and toxic organic electrolytes, avoid the potential safety issue and environment concern; (ii) Easy to prepare. Aqueous system batteries don't need rigorous manufacturing conditions, and the price of electrolyte solvent and salt also cheap; (iii) high ion conductivity. The ion conductivity of the aqueous electrolyte is higher than those of organic electrolyte by 2 orders of magnitude [79]. So, TiHCF electrode material was first tested in aqueous electrolyte.

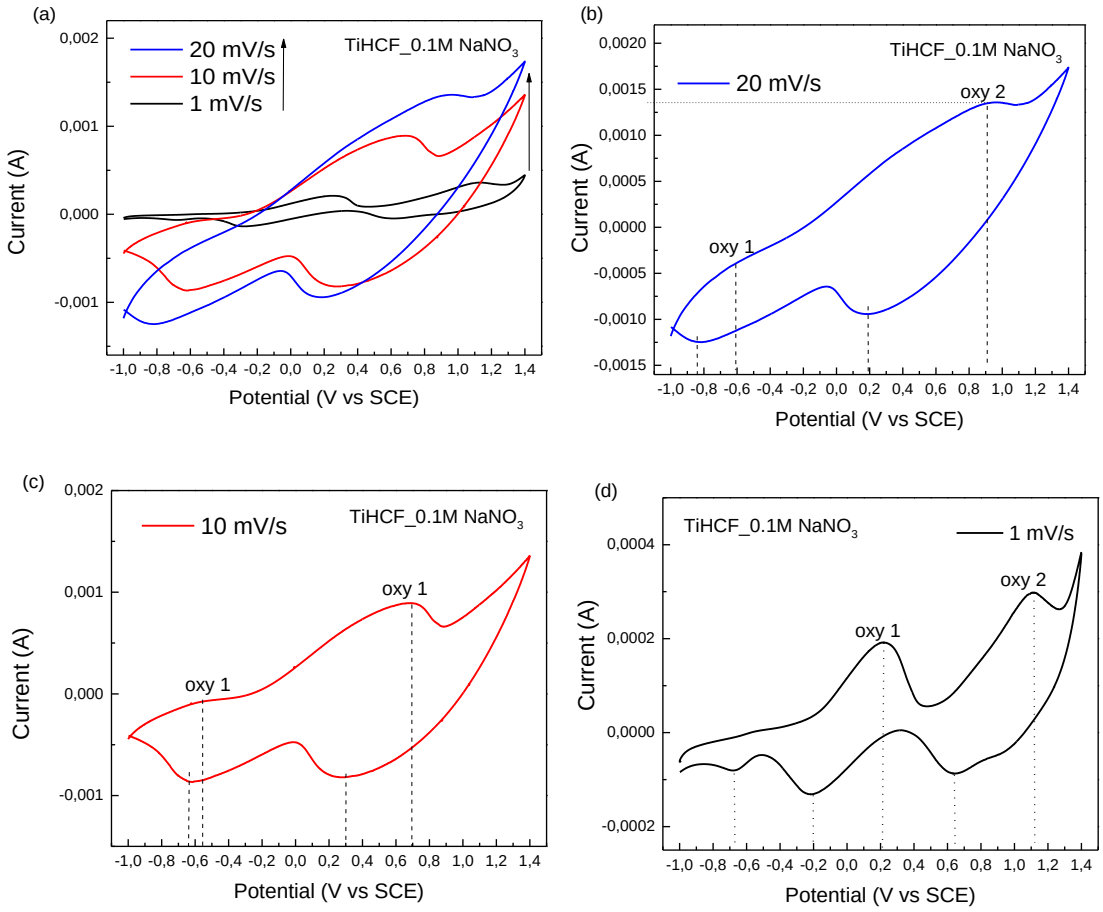

Figure 22. Cyclic voltammetry of TiHCF in 0.1M $NaNO_3$ electrolyte at different scan rate.

A shown in figure 22 in 0.1M $NaNO_3$ electrolyte, Cyclic voltammetry (CV) curves were recorded at different scan rates in the voltage range from -1.0 to 1.3V. At least a couple peaks in both oxidation and reduction is observed, depending on the applied scan rate. While applying a fast scan rate such as 20mV/s and 10mV/s, the electrolyte does not have enough time to fully insert to electrode material, and therefore the definition (also separation) of the oxydo-reduction peaks is less evident. Even though we still found that the system undergoes double reduction and double oxidation in $NaNO_3$ electrolyte, but only one apparent oxidation peak around 0.7V. By applying 1mV/s scan rate, three pairs of redox peaks were found at voltage range around -0.7~0.5V, -0.2-0.2 V and 0.65-1.1 V. According to the report about PBAs electrode material in aqueous Na-ion system, for instance, Bianca Paulitsch et al [87] reported $Na_2VO_x[Fe(CN)_6]$ was used electrode material in 1 M Na_2SO_4 + 3.6 M H_2SO_4 solution, and a main peak around 0.9V was attributed to the redox of $Fe^{3+/2+}$ pair. Meanwhile they also compared the potential of $Fe^{3+/2+}$ pair when B position in $Na_2B[Fe(CN)_6]$ was substituted by different metals: B = Ni, Co, Cu and VOx in 0.25M Na_2SO_4 aqueous solution, and shown the order VOx (0.9V) >Cu (0.63V) >Co(0.46V) >Ni (0.4V), as shown

in figure 23. From this report, we can postulate than the peak of TiHCF around 1.1V attribute to $Fe^{3+/2+}$, and the peaks around -0.2~0.2V should attribute to $Ti^{4+/3+}$.

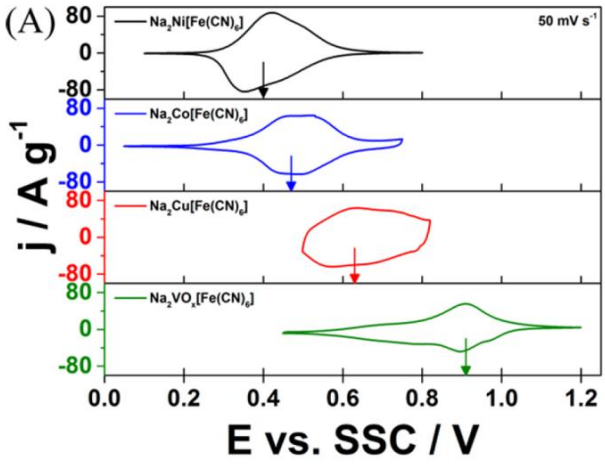

Figure 23. Typical CVs for sodium intercalation/deintercalation in the case of $Na_2B[Fe(CN)_6]$ (B = Ni, Co, Cu and VOx) in 0.25 M Na_2SO_4 aqueous electrolytes from reference [87].

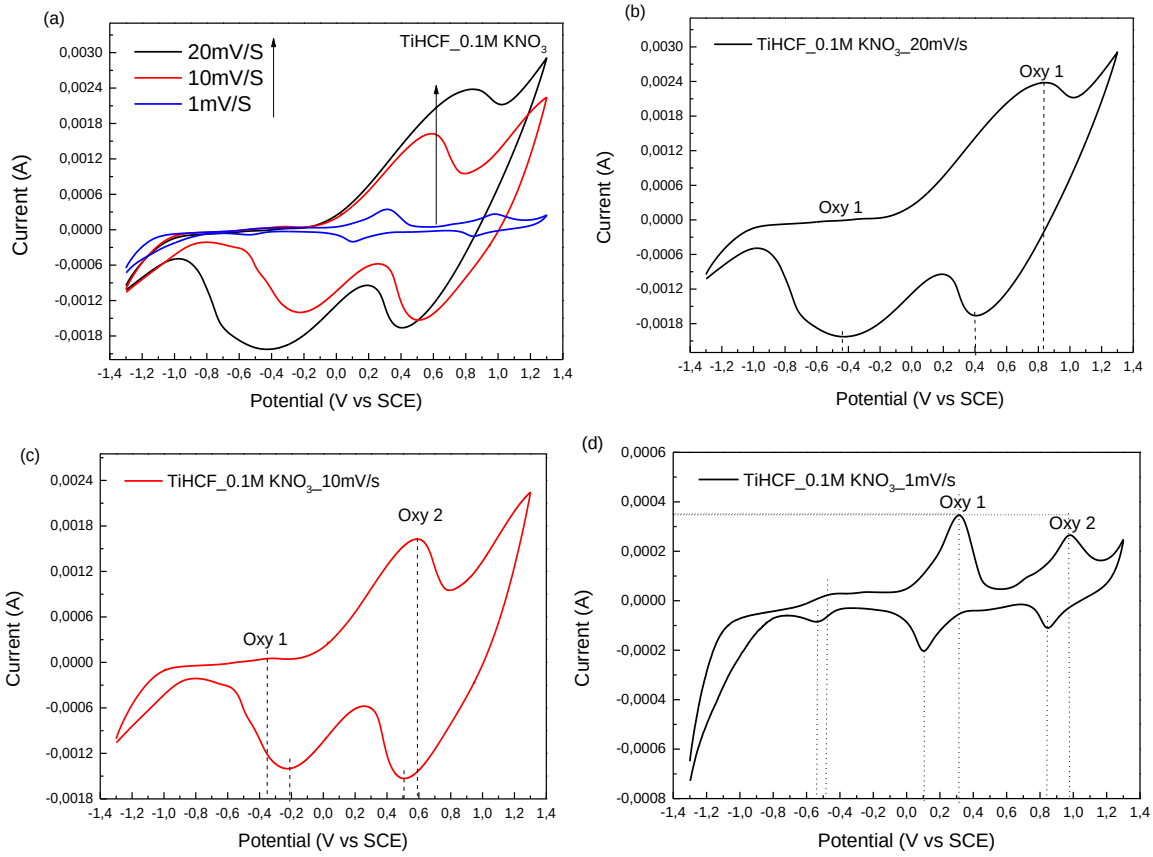

Figure 24. Cyclic voltammetry of TiHCF in 0.1M KNO_3 electrolyte at different scan rate.

Except aqueous $NaNO_3$ electrolyte, the as-prepared sample was also been tested in 0.1M KNO_3 solution, and the results are shown in figure 24. Cyclic voltammetry (CV) curves were recorded in the voltage range from -1.3 to 1.3V. From figure 24 (a), we found that CV curves in KNO_3 electrolyte are very similar with those in $NaNO_3$ solution. At fast scan rate, the system undergone double reduction and double oxidation, but only one oxidation peak around 0.6V was apparent. When we use 1mV/s scan rate, three pairs of redox peaks were found at voltage range around -0.6~0.5V, 0.2-0.4 V and 0.65-1.1 V, and the dramatic increase of current at low potential (around -1.3V) was due to the reduction of solvent. The CV curve we got was very similar with the data of *Y. Luo et al* [88] reported, the difference is that they tested Potassium titanium hexacyanoferrate ($K_{0.3}Ti_{0.75}Fe_{0.25}[Fe(CN)_6]_{0.95}\cdot 2.8H_2O$) in organic electrolyte by using two electrode system, and they also saw three pair of peaks which are the redox couple of $Ti^{3+/4+}$ around 1.6/2.1V, and the other two around 3.6/3.2V and 4.3/3.7V, where the former peaks from the redox reaction on the Fe site with a high-spin configuration coordinated to nitrogen, and the later peaks from Fe site with low-spin configuration coordinated to carbon. Because the different electrolyte (aqueous electrolyte) and electrode system (three-electrode system) we used, we cannot refer the potential values from the reported paper, but we can conclude that Ti sites are active during the charge-discharge process, and we postulate that the peak around 0.2~0.4V attribute to $Ti^{4+/3+}$and the peaks around 1.1V attribute to $Fe^{3+/2+}$.

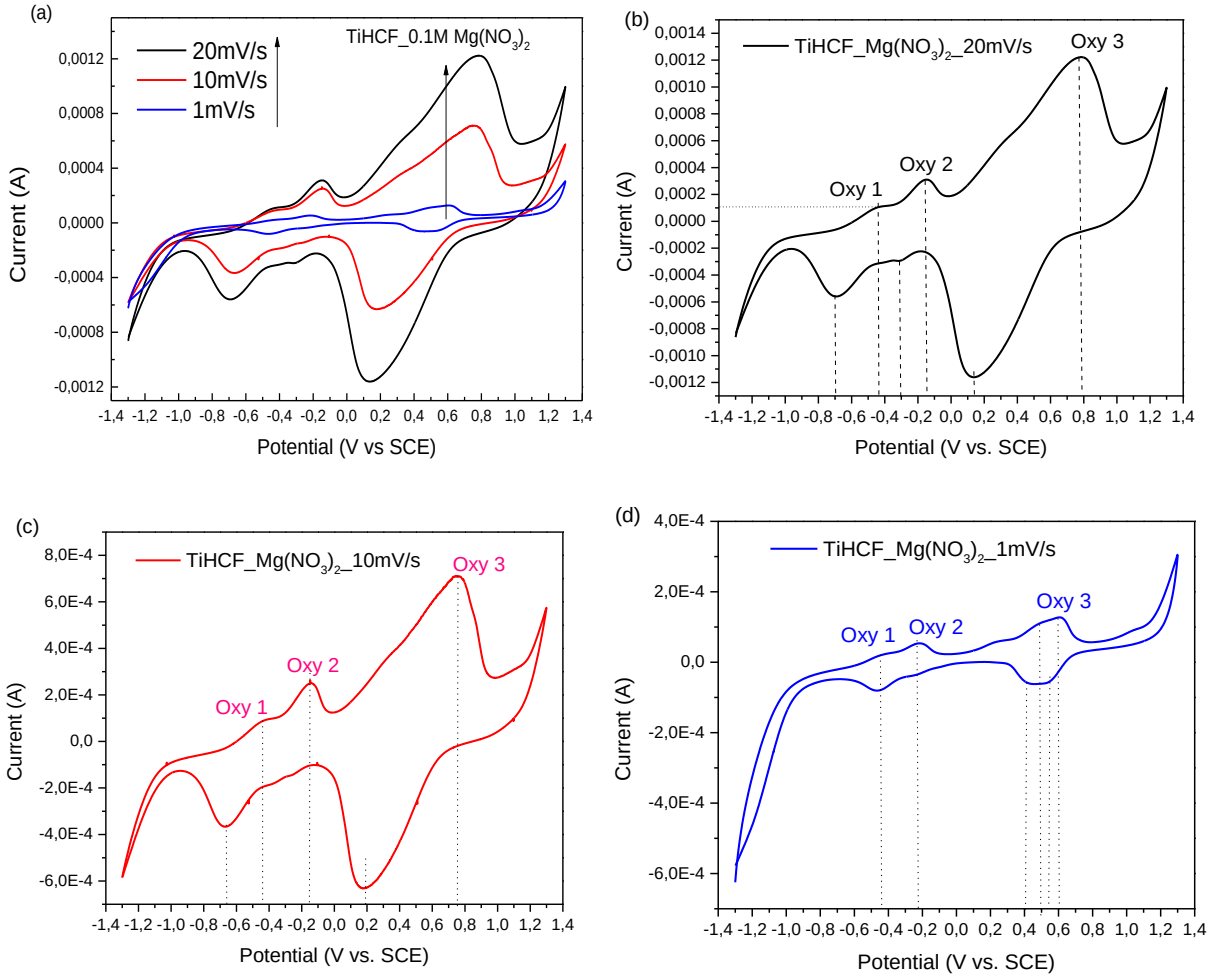

Figure 25. Cyclic voltammetry of TiHCF in 0.1M Mg $(NO_3)_2$ electrolyte at different scan rate.

In addition to the test in monovalent cation ion electrolyte, the as-prepared sample was also been tested in divalent cation 0.1M Mg $(NO_3)_2$ solution. As we mentioned before, Mg^{2+} possesses two valence electrons and has the lowest standard electrode potential (ca. -2.36 V vs. SHE) among the air-stable metals. Magnesium-ion batteries theoretically contain almost twice as much energy per volume as lithium-ion batteries (32.731 GJ/m^3 vs. 22.569 GJ/m^3) [42, 43]. So, we are interested in testing of our material in Mg-ion electrolyte.

As shown in figure 25, the cyclic voltammetry curves were recorded in the voltage range from -1.3 to 1.3V. From figure 25(a), we found that when we decrease the scan speed from 20mV/s to 1mV/s, the oxidation peaks move from high potential to lower potential and the reduction peaks move from low potential to high potential, and at last shown four pairs of well symmetrical peaks at potential around 0.4~0.6V, -0.2V, -0.5V and at scan rate of 1 mV/s. We noticed that the oxidation peak around 0.75V at 10 mV/s separates to two peaks at 1 mV/s. This maybe because of the different coordination states (Ti vacancies or coordinated water) around Fe atom. But it's difficult

to specify the four pairs of redox peaks only by the voltammetry. According to the report of Yagi et al [56] about the cyclic voltammograms for CuFe-PBA electrode in 1.0 M $MgSO_4$, there were three pairs of peaks (around 0.38V and 0.80V and 1.02V) been observed, however possible electrochemical active redox couples are two pairs, i.e. Fe ^{III}/Fe ^{II} and Cu ^{II}/Cu ^{I}. They found during the charge and discharge process, not only cations but also anions, contribute to the charge compensation in aqueous electrolyte, and resulting in redox peak splitting. Here, except the redox pairs of $Ti^{3+/4+}$ and $Fe^{3+/2+}$, we do not confirm whether NO_3^- ions participate in the reaction.

Table 4. Current value of oxidation peaks at different scan rate in Mg $(NO_3)_2$ electrolyte.

Scan speed (mV/s)	Current (A)		
	Oxy 1	Oxy 2	Oxy 3
1	0.000022	0.000060	0.000114
10	0.000100	0.000025	0.000714
20	0.000110	0.000314	0.001229
b value	0.56	0.57	0.54

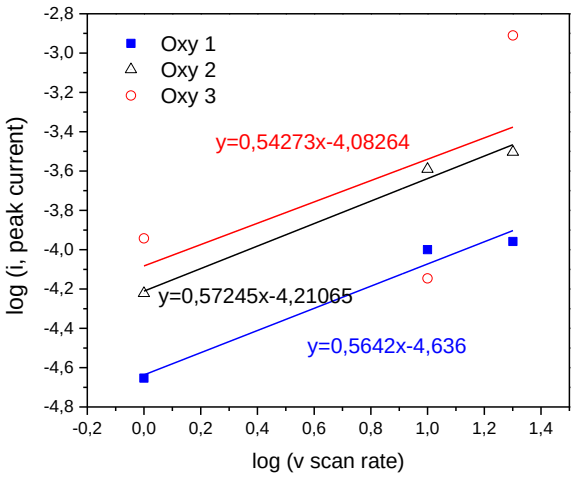

Figure 26. log(i) versus log (v) plots of different oxidation peaks in Mg $(NO_3)_2$ electrolyte.

Additional kinetic information on the electrochemical mechanism of the Mg^{2+} insertion in the studied electrode can be revealed by looking at the peak current variation as a function of the scan rate. According to the empirical power-law relationship, the scan rate and peak current of CV can be written as: $i=av^b$……equation (3)

where i is the current, v is the scan rate, and a and b are the adjustable parameters. When we plot log (i) vs. log (v) curve, we can get b values from the slope. These b values indicate that the capacity of the as-prepared sample is controlled by capacity (b=1) or diffusive (b=0.5) processes. From figure 26, we can see that, for the three oxidation peaks observed in CV curves of TiHCF in Mg $(NO_3)_2$ electrolyte, the b values are 0.56, 0.57 and 0.54, respectively. During the calculation of b values, we saw that oxidation peak 1 and peak 2 show good linear ship within different scan rate; but peaks 3 shown discrete distribution, this maybe because of the splitting of peaks around oxidation peaks 3, here we suppose it is only one peak, and the calculation was based on the current of the highest peak (around 0.6V). All the b values indicate that the capacity of as-prepared sample TiFCF is diffusion-controlled process in Mg $(NO_3)_2$ electrolyte. It means inside the crystal structure, the A-sites are inserted or extracted with Mg-ion during the charge-discharge process here, as shown in figure 6. The same calculation also holds for $NaNO_3$ and KNO_3 electrolyte.

Table 5. Current value of oxidation peaks at different scan rate in $NaNO_3$ and KNO_3 electrolyte.

Scan speed (mV/s)	Current (A) in $NaNO_3$ electrolyte	
	Oxy 1	Oxy 2
20	-0.00044	0.0014
10	-0.000004167	0.0090
1	0.00025	0.0003
b value	2.98 #	0.50
Scan speed (mV/s)	Current (A) in KNO_3 electrolyte	
	Oxy 1	Oxy 2
1	0.000350	0.00030
10	0.000025	0.00168
20	0.000001	0.00252
b value	-1.75 #	0.72

Oxidation peak was too weak to get exact current value at high scan rate.

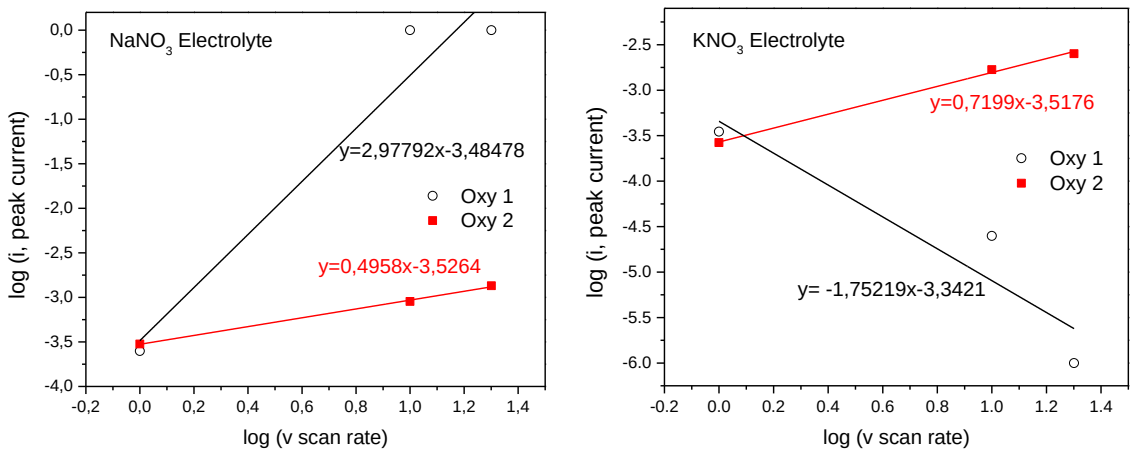

Figure 27. log (i) versus log (v) plots of different oxidation peaks in $NaNO_3$ and KNO_3 electrolyte.

There are mainly two oxidation peaks were observed from the CV curves in $NaNO_3$ and KNO_3 electrolyte, we listed the current values at different scan rate, as shown in table 5. But we found there are problems for the oxidation peak 1 in both $NaNO_3$ and KNO_3 electrolyte, because of the weakness of this peaks, we cannot get the exactly current value. So, we only refer the b value got from oxidation peak 2 here. From figure 27, we got the b values are 0.50 for $NaNO_3$ electrolyte and 0.72 for KNO_3 electrolyte. It indicates that the capacity in $NaNO_3$ electrolyte is controlled by diffusion process, and the capacity in KNO_3 electrolyte is controlled by both diffusion and capacitive processes. It means during the charge-discharge process, Na-ions and K-ions also shown insertion or extraction behavior in the A-site. For the K-ions only, the mechanism is also capacitive and therefore K^+ ion accumulation at the surface of the electrode is postulated.

4.2 Organic electrolyte system

Different with aqueous electrolyte, organic electrolytes show the advantage of wide potential window. According to the specific energy density and power equations (4/5): the higher voltage range we have, the higher energy density and power density we will get. So, except the aqueous electrolyte systems, we also assembled Li/Na-ion coin cells by using 1M $LiPF_6$/EC-DMC (1:1) and 1M $NaPF_6$ in PC as electrolyte.

$$E(Wh/kg) = C(mAh/g) * V(V) \quad \text{..... equation (4)}$$

$$P\ (W/kg) = \frac{E}{C-rate} \text{.....equation (5)}$$

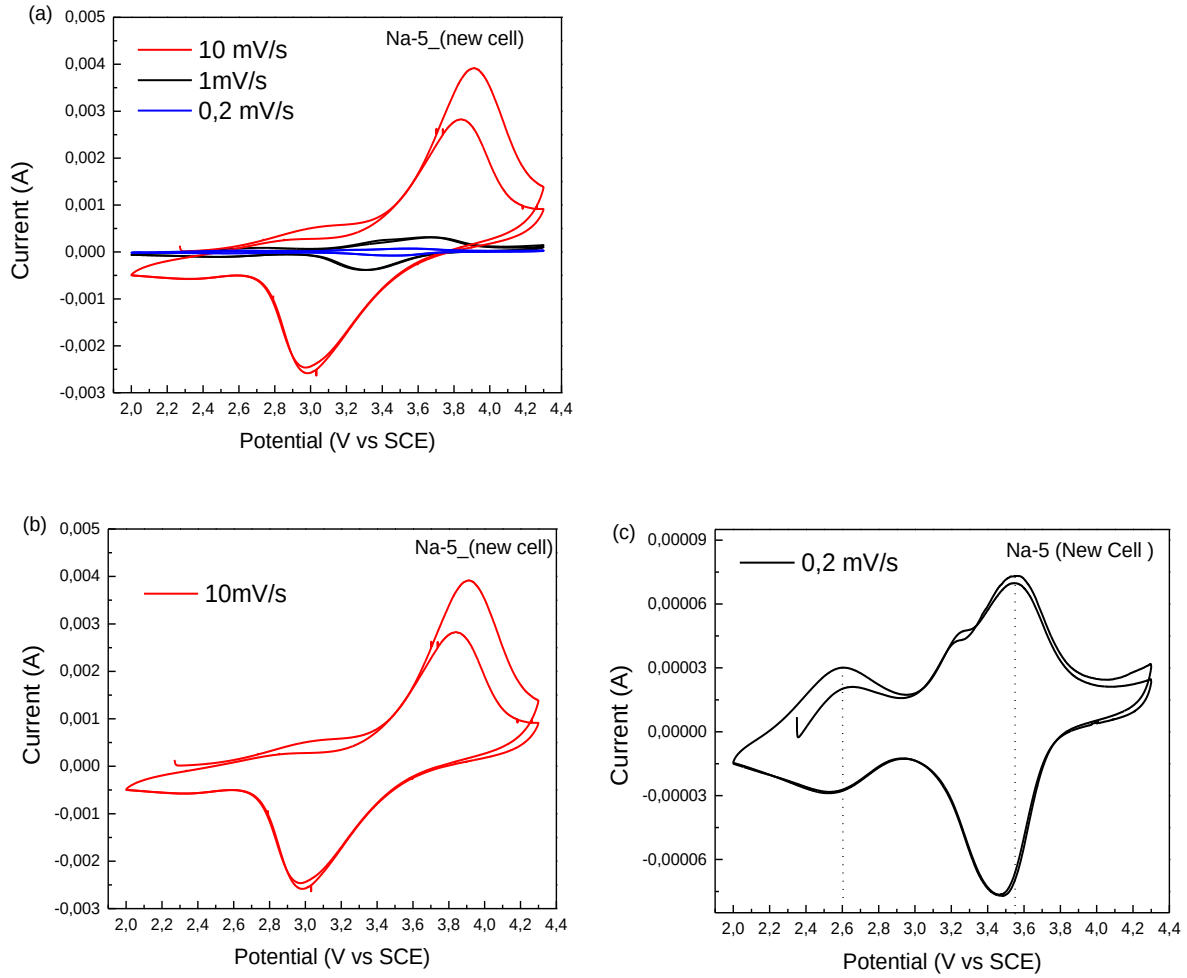

Figure 28. Cyclic voltammetry of TiHCF Na-ion coin cell in $NaPF_6$ electrolyte at different scan rate.

Figure 28 shows the Cyclic voltammetry curves of Na-ion coin cell at different scan rate. When we applied high scan speed, one pair of apparent redox peaks was observed at around 3.0/3.9V, except that there is a week oxidation peak at around 3.1V was noticeable. But when we decrease the scan speed from 10 mV/s to 0.2 mV/s, we found that the oxidation peaks removed to lower potential and the reduction peaks move to high potential. As show in figure 26 (c), two pair of perfect symmetry peaks at around 2.6V and 3.6V were observed at 0.2 mV/s. According to the Xie et al., the CV curves of sodium titanium hexacyanoferrate ($Na_{0.66}Ti[Fe(CN)_6]_{0.92}\cdot\square_{0.08}$, □ vacancy in the framework) in $NaPF_6$+EC+DC electrolyte shown two main characteristic pairs of redox peaks: oxidation/reduction of the high-spin $Ti^{3+/4+}$ couple (3.0/2.6V) and low spin $[Fe(CN)_6]^{4-/3-}$ couple (3.4/3.2V), respectively [89]. So, according to this report, we attribute the redox peak at around 2.6V to $Ti^{3+/4+}$ couple, and the redox peak around 3.5/3.6V to $Fe^{2+/3+}$.

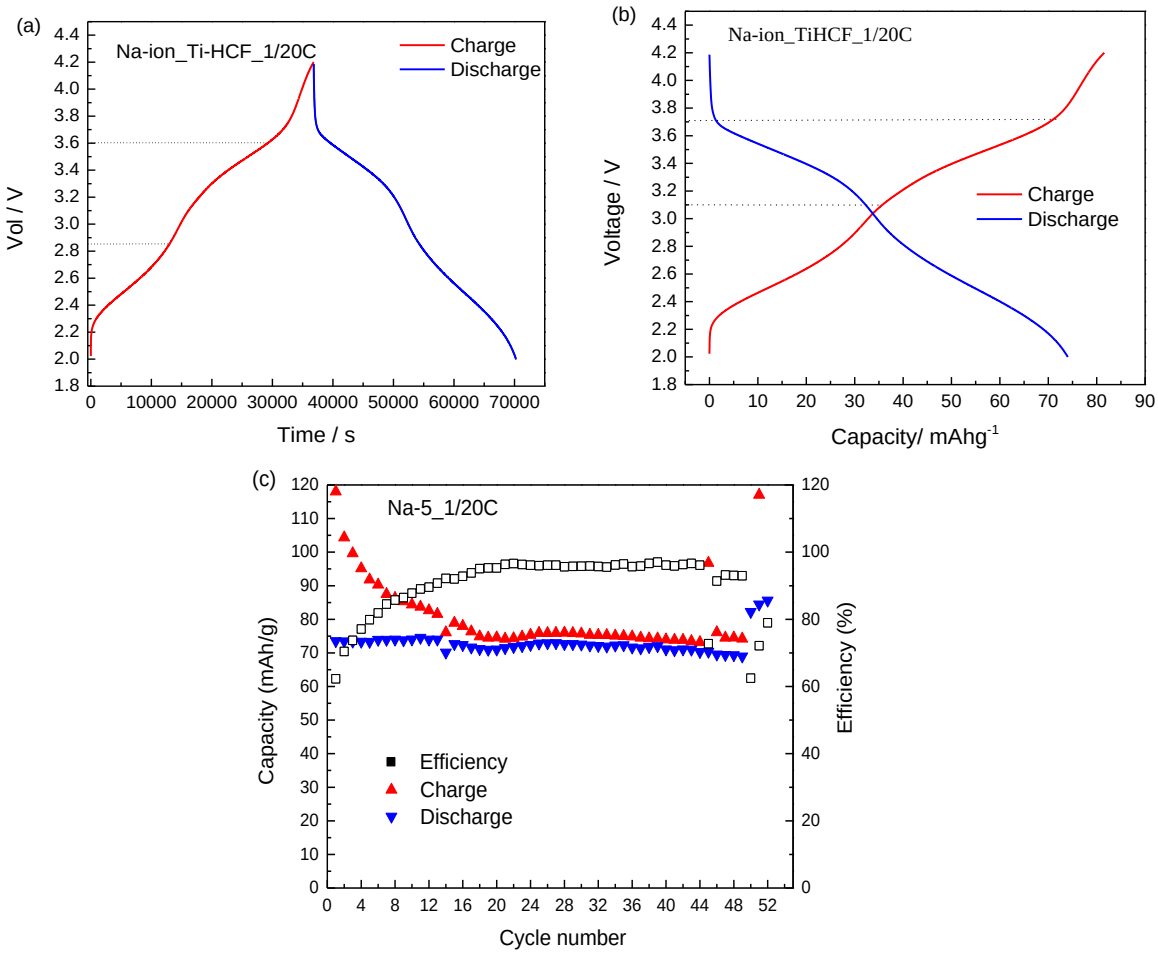

Figure 29 Galvanostatic initial charge and discharge curves of Na-ion coin cells: (a) Potential-time plot; (b) Potential-capacity plot; (c) Cycling performance of TiHCF at C/20 between 2.0-4.2V.

Figure 29 shows the galvanostatic charge discharge curve of TiHCF with a current of C/20 in the range of 2.0-4.2V vs. Na^+/Na. According to potential-time curve, we can calculate the capacity by using the equation: $C=I*\Delta t/m$ ……equation (6).

As shown in figure 29(b), the discharge capacity is around 74 mAh/g. The theoretical capacity of $Na_{0,86}\ Ti_{0,73}[\ Fe(CN)_6]\cdot 3H_2O$ can be calculated as 83.6 mAh/g (considering 1 mol of Na^+ per unit formula). By considering here that only 0.86 mol of Na^+ participate in the reaction, the capacity should be 0.86*83.6=71.9 mAh/g. Therefore, during the charge and discharge process, all the available Na^+ ions participate to the reaction. Additionally, the charge and discharge curves are characterized by a two-step processes, without any indication of a well-defined flat plateau. This may indicate the presence of a non-negligible portion of amorphous structure of our sample, which is consistent with the XRD result. Figure 29 (c) shows the cycling performance of TiHCF, and the framework exhibits excellent capacity retention, more than 95% discharge capacity is retained after

50 cycles. We noticed that the cell shows a low coulombic efficiency at the initial cycling, and after 20 cycles, the coulombic efficiency reached a stable value and keep around 95%. According to the report of Yuhao Lu et al [22], the most probable cause for such a low coulombic efficiency at beginning is the crystalline water in the compound. The large interstitial spaces in PBA readily absorb water molecular. Decomposition of the residual water during the charge process would cause a low efficiency. With subsequent cycling, the amount of residual water would decrease, and the efficiency increase.

According to equation (4), the specific energy of this Na-ion coin cell is around: 74 mAh/g *3.4 V ≈ 250 Wh/kg (based on the mass of active material), and this value is very close to the date reported by Yuhao Lu et al in 2012, of MnHCF, CoHCF, NiHCF and CuHCF, and even higher than ZnHCF electrode material, which tested in saturated $NaClO_4$ in 1:1 EC/DEC (vol.:vol.) electrolyte [22].

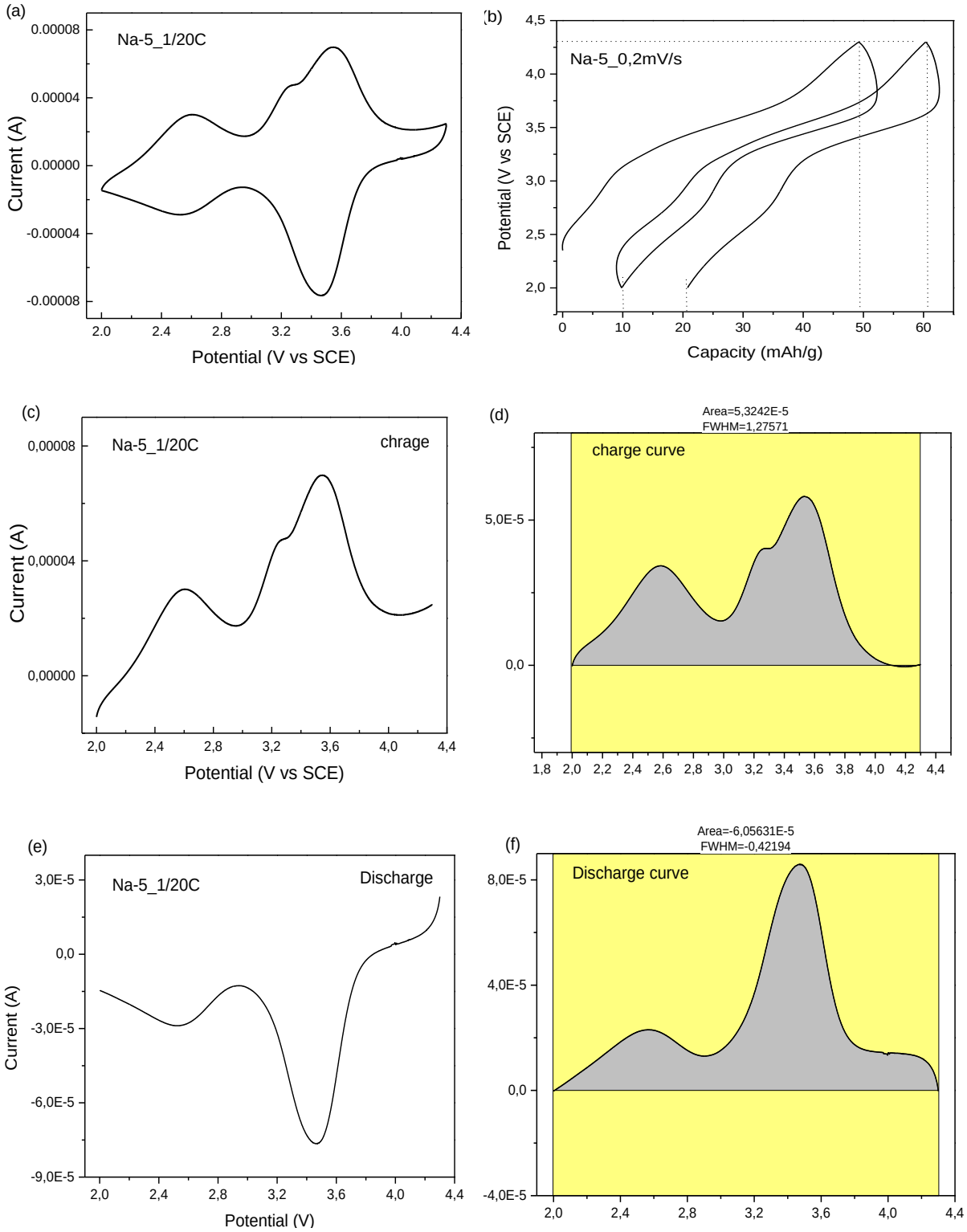

Figure 30 (a) CV curve of TiHCF at 0.2 mV/s; (b) capacity calculated by CHI software; (c) Charge curve of TiHCF CV at 0.2 mV/s; (d)* Integration of Charge curve of TiHCF CV at 0.2 mV/s; (e) Discharge curve of TiHCF CV at 0.2 mV/s; (f)* Integration of Discharge curve of TiHCF CV at 0.2 mV/s;

* (d) (f) manual integration (using Origin software).

For the calculation of battery specific capacity, we rely here on two methods: i) based on the galvanostatic charge/discharge test; ii) calculated from CV curve by doing the integration of charge and discharge curve, based on the equation (7), as shown in figure 30 (b) (d) (f). In particular, figure 30(b) reports data from CHI software directly. In addition, Figure 30, panels (d) and (f) report data calculated (integrated) by Origin. The integrals were made by applying the formula $\int$ IdV, obtaining the following capacity values for charge and discharge, respectively: 37.9 mAh/g and 43.1 mAh/g, at scan rate of 0.2 mV/s. As shown in table 6, the discharge capacities from method ii) were really close, 40 mAh/g and 43.1 mAh/g, respectively.

$$Capacity\ (mAh/g) = \frac{\int \mathrm{IdV}}{3.6*v*m} \quad \text{.....equation (7)}$$

where I is current; dv is the voltage range; v is scan rate; m is mass of active material.

Table 6. Capacity values calculated according to CV curve and Galvanostatic charge/discharge curves.

	CV curve 0.2 mV/s		
	integration did by CHI software	Integration did by origin	
	Capacity (mAh/g)	Area	Capacity (mAh/g)
Charge curve	50	$5.3242*10^{-5}$	37.9
Discharge curve	40	$6.05631*10^{-5}$	43.1

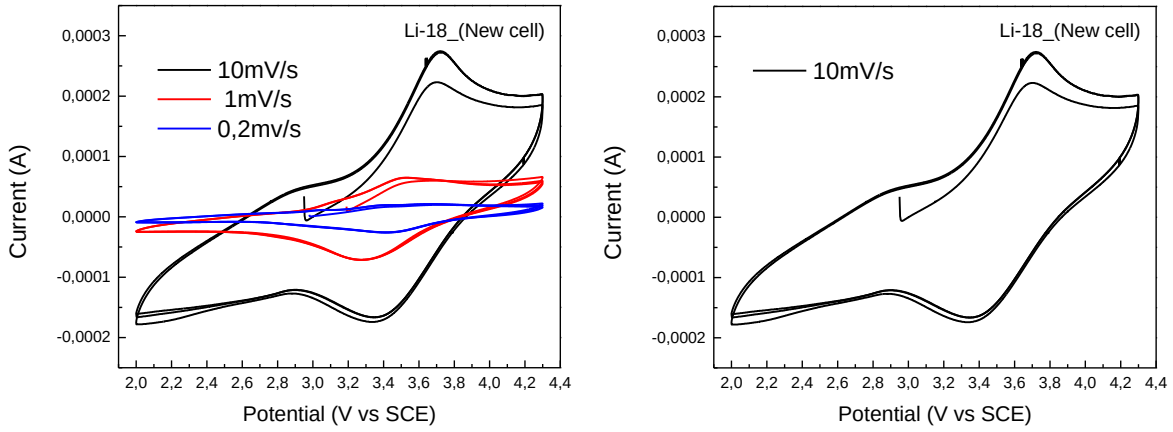

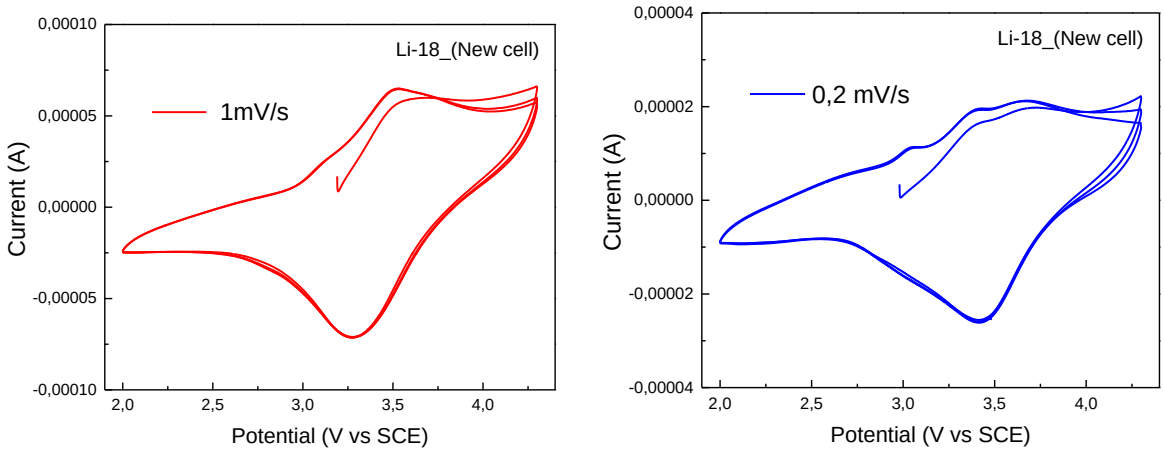

Figure 31 Cyclic Voltammetry of TiHCF Li-ion coin cell in $LiPF_6$ electrolyte at different scan rate.

Figure 31 shows the CV curves of Li-ion coin cells of TiHCF. At high scan speed 10 mV/s, it shows the similar peaks with Na-ion coin cells, with one pair of apparent redox peaks around 3.4/3.7V, and a weak oxidation peak at around 2.9V. But when we decrease the scan speed from 10 mV/s to 0.2 mV/s, we found that the oxidation peak at 3.7V moved to low potential and separates into two peaks. According to the report of Yagi et al [56], during the charge and discharge process, not only cations but also anions, contribute to the charge compensation in aqueous electrolyte, and resulting in redox peak splitting. Meanwhile they also first reported the electrochemical adsorption /desorption of PF_6^- ions occurs in addition to the insertion/extraction of Li^+ ions upon the redox reaction of PB, as shown in figure 32. The cyclic voltammogram also clearly indicates the presence of anodic peaks for the adsorption of PF_6^- ions and the extraction of Li^+ ions during the anodic sweep [90]. Base on this report, we cannot ascertain that there is PF_6^- ions participate in the reaction, but from the splitting of peaks around 3.7V ($Fe^{3+/2+}$), we can postulate that there is different environment conditions for titanium site (vacancies or coordinated water) which coordinated to Fe site.

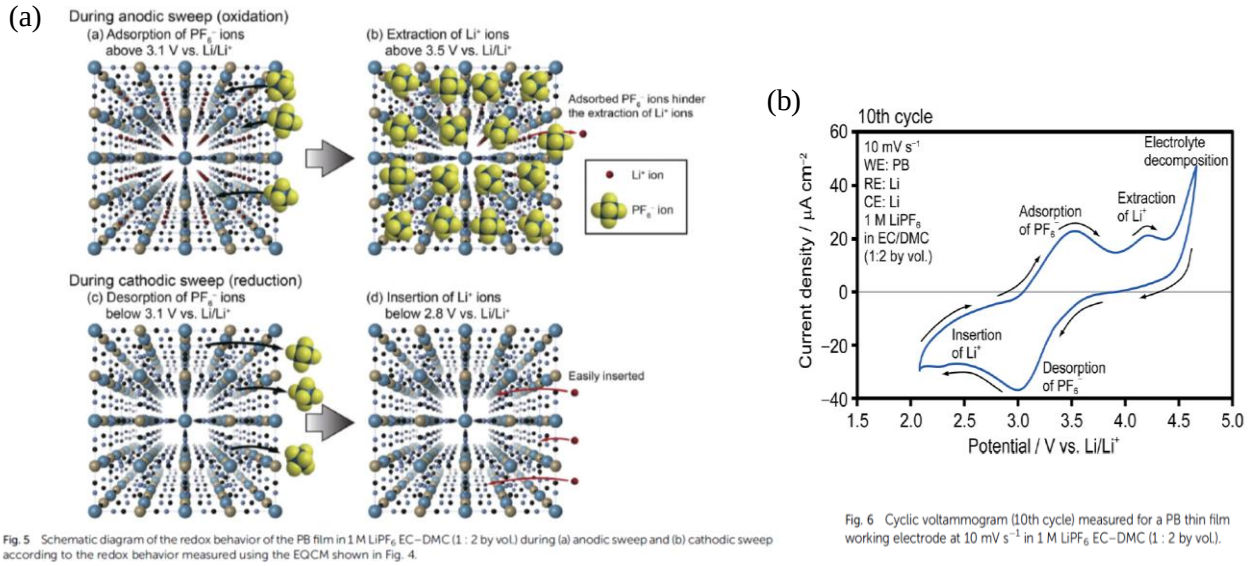

Fig. 5 Schematic diagram of the redox behavior of the PB film in 1 M $LiPF_6$ EC–DMC (1 : 2 by vol.) during (a) anodic sweep and (b) cathodic sweep according to the redox behavior measured using the EQCM shown in Fig. 4.

Fig. 6 Cyclic voltammogram (10th cycle) measured for a PB thin film working electrode at 10 mV s^{-1} in 1 M $LiPF_6$ EC–DMC (1 : 2 by vol.).

Figure 32 (a) Schematic diagram of the redox behavior of the PB film during anodic and cathodic sweep; (b) cyclic voltammogram of PB thin film at 10 mV/s in 1M $LiPF_6$ EC-DMC (1:2 by vol) from reference [90].

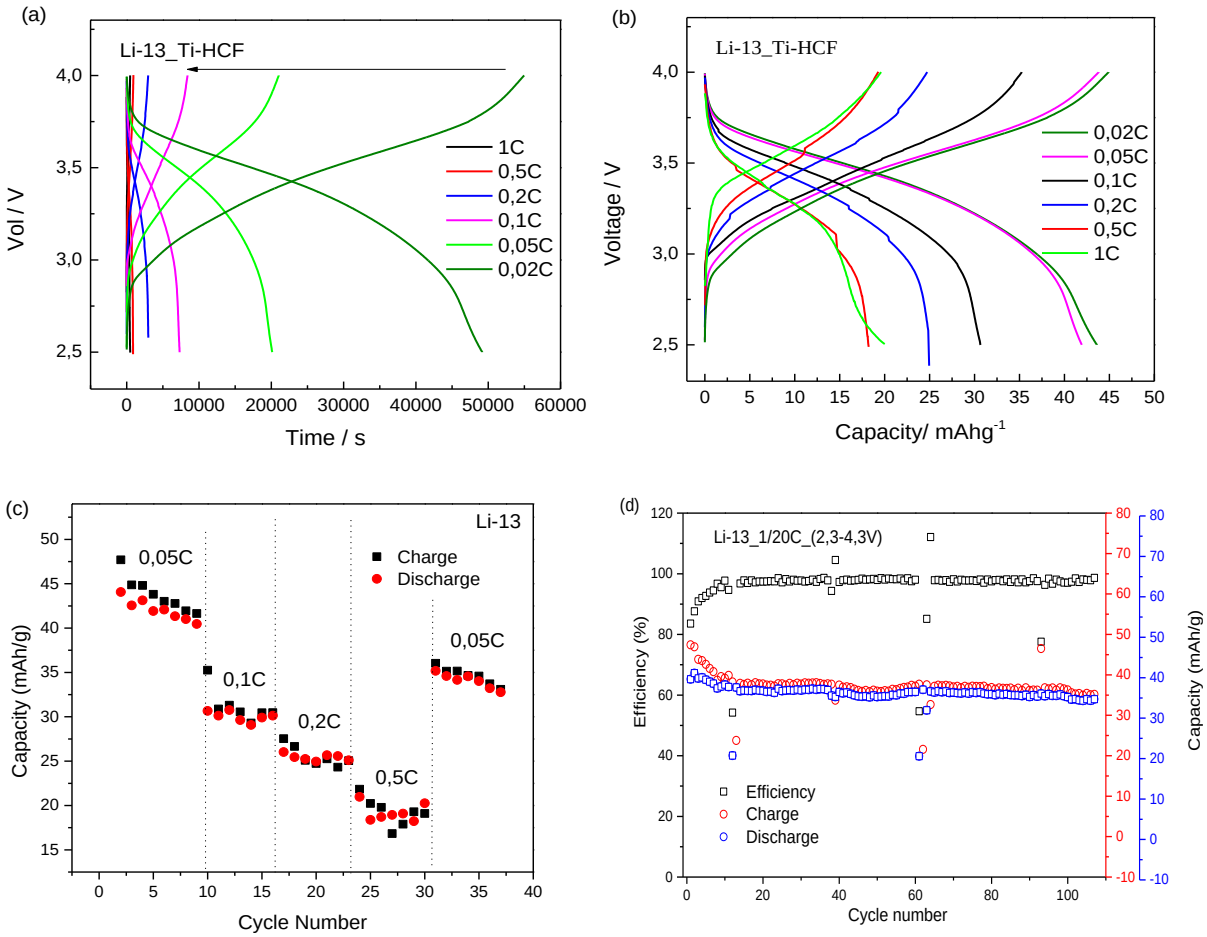

Figure 33. Galvanostatic initial charge and discharge curves of Li-ion coin cells: (a) Potential-time plot; (b) Potential-capacity plot; (c) Cycling performance of TiHCF at C/20 between 2.0-4.2V.

Figure 33 show the galvanostatic curve Li-ion coin cell of TiHCF at different C-rate in the range of 2.5-4.0V vs. Li^+/Li. According to potential-time curve, we can calculate the capacity by using the equation: $C=I*\Delta t/m$ (6). We also got the capacity value directly from the experiment (figure 33 (b)), the discharge capacity is around 45 mAh/g at 0.02C. Figure 33 (c) shows the capacity values at different C-rate after 10 cycles, the capacity was around 45 mAh/g at beginning and decreased to 40 mAh/g after 10 cycles at 0.05C, then after the cycles at 0.1C, 0.2C and 0.5C, the retained capacity at 0.05C reached 77% of the initial maximum capacity. So, it indicates that after the cycles at high C-rate, there is a fading for the delivered capacity, and this probable due to some irreversible reaction happened during cycling. According to equation (4), we can get the specific energy of Li-ion coin cells, about 35 mAh/g * 3.5V ≈ 122 Wh/Kg, which significantly lower than the value of Na-ion coin cell. After that we did the cycling test at 0.05C, TiHCF retained 96.6% capacity after 100 cycles with high coulombic efficiency of nearly 100% (figure 33 (d)).

V. Conclusion

In this work, Prussian blue analogue -Titanium hexacyanoferrate (TiHCF) has been synthesized by simple co-precipitation method, and the as-prepared sample was characterized by PXRD, FT-IR, TGA, MP-AES and XAS. The obtained material TIHCF has the chemical formula of $Na_{0,86}$ $Ti_{0,73}$[Fe $(CN)_6$] · $3H_2O$, with cubic structure (space group: p m-3 m). From XAS data, we conclude that there is distortion for the local Ti sites and the bond distances of Ti-N, Ti—C and Ti---Fe are 1.7 Å, 2.9 Å and 4.7 Å, respectively.

The as-prepared sample show good performance in electrochemical test. First, the sample was tested in aqueous system; we observed redox peaks of both $Fe^{3+/2+}$ and $Ti^{4+/3+}$ pairs from cyclic voltammetry curves. From the calculation result based on scan rate and current, we conclude that the capacity of battery is controlled by diffusion process. It indicates that the cationic ions (Na^+, K^+, Mg^{2+}) insert inside the crystal structure (A-site) during discharge process.

Meanwhile, we also tested our sample in organic electrolyte system for Li-ion and Na-ion batteries. Because the precursor we used for synthesis is Na_4Fe $(CN)_6$, Na is first removed from the structure during the first charge. Experiments shown that the material displays higher capacity for Na-ion batteries (74 mAh/g at C/20 rate) respect to Li-ion batteries (35 mAh/g at the same rate). The specific energy value obtained for Na-ion coin cell reaches 250 Wh/kg (based on the mass of active material) and 122 Wh/kg for Li-ion coin cell, which are in line, and slightly better, than those of other battery technology (figure 38). Both Li-ion and Na-ion cells show high coulomb efficiency during cyclability test, above 95%.

VI. References

[1]. D. Sprake, Y. Vagapov. Housing Estate Energy Storage Feasibility for a 2050 Scenario. Conference: 7th International Conference on Internet Technologies and Applications At: Wrexham, UK. DOI: 10.1109/ITECHA.2017.8101925.

[2]. J. Song, L. Wang, Y.h.Lu, J. Liu, B.k. Guo, P.h. Xiao, J.-J. Lee, X.-Q. Yang, G. Henkelman, J. B. Goodenough. Removal of Interstitial H_2O in Hexacyanometallates for a Superior Cathode of a Sodium-Ion Battery. J. Am. Chem. Soc. 2015, 137, 2658-2664.

[3]. M. S. WHITTINGHAM, Electrical Energy Storage and Intercalation Chemistry. Science,1976, Vol. 192, Issue 4244, pp. 1126-1127. DOI: 10.1126/science.192.4244.1126.

[4]. Keywords to understanding Sony Energy Devices- keyword 1991".

[5]. Monthly battery sales statistics. Machinery statistics released by the ministry of economy, trade and industry, March 2011.

[6]. S. S. Liang, W.q. Yan, X. Wua, Y. Zhanga, Y.s. Zhua, H.w. Wang, Y.p. Wu. Gel polymer electrolytes for lithium ion batteries: Fabrication, characterization and performance. Solid State Ionics, 2018, 318, 2-18.

[7]. K. C. Kam, M. M. Doeff. Electrode Materials for Lithium Ion Batteries. Material Matters, 2012, 7, 4.

[8]. A. Mishra, A. Mehta, S. Basu, S. J. Malode, N. P. Shetti , S. S. Shukla, M. N. Nadagouda, T. M. Aminabhavi. Electrode materials for lithium-ion batteries. Materials Science for Energy Technologies, 2018, 1, 182-187.

[9]. T. Matsuda, M. Takachi, Y. Moritomo. A sodium manganese ferrocyanide thin film for Na-ion batteries. Chem. Commun., 2013, 49, 2750-2752.

[10]. Battery energy storage. White paper. SUSCHEM BATTERY ENERGY STORAGE WHITE PAPER.

[11]. R. D. Shannon, Revised effective ionic radii and systematic studies of interatomic distances in halides and chalcogenides, Acta Cryst. (1976). A32, 751-767. https://doi.org/10.1107/S0567739476001551.

[12]. J.Y. Hwang, S.T. Myung, Y.K. Sun. Recent Progress in Rechargeable Potassium Batteries. Adv. Funct. Mater. 2018, 28, 1802938.

[13]. A. S. Nagelberg, W. L. Worrell. A thermodynamic study of sodium intercalated TaS_2 and TiS_2. J. Solid State Chem., 1979, 29, 345-354.

[14]. J.Y. Hwang, S.T. Myung, Y.K. Sun. Sodium-ion batteries: present and future. Chem. Soc. Rev., 2017, 46, 3529-3614.

[15]. C. Delmas. Sodium and Sodium-Ion Batteries:50 Years of Research. Adv. Energy Mater., 2018,8, 1703137.

[16]. R. Berthelot, D. Carlier-Larregaray, C. Delmas. Electrochemical investigation of the P2–Na_xCoO_2 phase diagram. Nat. Mater., 2011,10, 74.

[17]. M. Guignard, C. Didier, J. Darriet, P. Bordet, E. Elkaim, C. Delmas. P2-NaxVO2 system as electrodes for batteries and electron-correlated materials. Nat. Mater., 2013, 12, 74.

[18]. L. Vitoux, M. Guignard, M. Suchomel, J. Pramudita, N. Sharma,C. Delmas. The Na_xMoO_2 Phase Diagram ($^1/_2 \leq x < 1$): An Electrochemical Devil's Staircase. Chem. Mater., 2017, 29, 7243.

[19]. C. Delmas, F. Cherkaoui, A. Nadiri, P. Hagenmuller. A nasicon-type phase as intercalation electrode: $NaTi_2(PO_4)_3$. Mater. Res. Bull., 1987, 22, 631.

[20]. J. Gopalakrishnan, K. Rangan. Switching Redox-Active Sites by Valence Tautomerism in Prussian Blue Analogues $A_xMn_y[Fe(CN)_6]\cdot nH_2O$ (A: K, Rb): Robust Frameworks for Reversible Li Storage. Chem. Mater., 1992, 4, 745.

[21]. N. Imanishi, T. Morikawa, J. Kondo, Y. Takeda, O. Yamamoto, N. Kinugasa, T. Yamagishi. Lithium intercalation behavior into iron cyanide complex as positive electrode of lithium secondary battery. J. Power Sources, 1999, 79, 215.

[22]. Y. H. Lu, L. Wang, J. G. Cheng, J. B. Goodenough. Prussian blue: a new framework of electrode materials for sodium batteries. Chem. Commun., 2012, 48, 6544.

[23]. M.M. Doeff, Y. Ma, S.J. Visco, and L.c. De Jonghe. Electrochemical Insertion of Sodium into Carbon. J. Electrochem. Soc., 1993, 140, 12, L169-L170.

[24]. H. Kahlert, U. Retter, H. Lohse, K. Siegler, and F. Scholz. On the Determination of the Diffusion Coefficients of Electrons and of Potasstium Ions in Copper (II) Hexacyanoferrate (II) Composite Electrodes. J. Phys. Chem. B, 1998, 102, 8757-8765

[25]. Z.l. Jian, W. Luo, X.l. Ji. Carbon Electrodes for K‑Ion Batteries. J. Am. Chem. Soc., 2015, 137, 11566−11569.

[26]. S. Komaba, T.Hasegawa, M.Dahbi, K. Kubota. Potassium intercalation into graphite to realize high-voltage/high-power potassium-ion batteries and potassium-ion capacitors Electrochem. Commun., 2015, 60, 172.

[27]. Z. L. Jian, Z. Y. Xing, C. Bommier, Z. F. Li, X. L. Ji. Hard Carbon Microspheres: Potassium-Ion Anode Versus Sodium-Ion Anode. Adv. Energy Mater., 2016, 6, 1501874.

[28]. A. Eftekhari. Potassium secondary cell based on Prussian blue cathode. Journal of Power Sources, 2004, 126, 221-228.

[29]. C. D. Wessells, S.V. Peddada, R. A. Huggins,Y. Cui. Nickel Hexacyanoferrate Nanoparticle Electrodes for Aqueous Sodium and Potassium Ion Batteries. Nano Lett., 2011, 11, 5421-5425.

[30]. C. D. Wessells, et al. Copper hexacyanoferrate battery electrodes with long cycle life and high power. Nat. Commun.2011, 2, 550. doi: 10.1038/ncomms1563.

[31]. C. Fouassier, C. Delmas, P. Hagenmuller. Evolution structurale et proprietes physiques des phases A X MO $_2$ (A = Na, K ; M = Cr, Mn, Co) ($x \leq 1$). Mater Res Bull, 1975, 10, 443-449.

[32]. C. Vaalma, G. A. Giffin, D. Buchholz, S. Passerini. Non-Aqueous K-Ion Battery Based on Layered $K_{0.3}MnO_2$ and Hard Carbon/Carbon Black. Journal of the Electrochemical Society, 2016, 163, 7, A1295-A1299.

[33]. H. Kim, J.C. Kim, S. H. Bo, T. Shi, D. H. Kwon, G. Ceder. K-ion batteries based on a P_2-type K $_{0.6}$ CoO $_2$ cathode. Adv Energy Mater, 2017, 7, 1700098.

[34]. C. Liu, S. Luo, H. Huang, Z. Wang, A. Hao, Y. Zhai, Z. Wang. K $_{0.67}$ Ni $_{0.17}$ Co $_{0.17}$ Mn $_{0.66}$ O $_2$: a cathode material for potassium-ion battery. Electrochem Commun., 2017, 82, 150-154.

[35]. K. Chihara, A. Katogi, K. Kubota, S Komaba. KVPO $_4$ F and KVOPO $_4$ toward 4 volt-class potassium-ion batteries. Chem Commun., 2017, 53, 5208-5211.

[36]. S. Komaba, T. Hasegawa, M. Dahbi, K. Kubota. Potassium intercalation into graphite to realize high-voltage/high-power potassium-ion batteries and potassium-ion capacitors. Electrochem Commun., 2015, 60, 172-175.

[37]. Z. Jian, W. Luo, X. Ji. Carbon electrodes for K-ion batteries. J Am Chem Soc., 2015, 137, 11566-11569.

[38]. W. Luo, J. Wan, B. Ozdemir, W. Bao, Y. Chen, J. Dai, H. Lin, F. Gu, V. Barone, L. Hu. Potassium ion batteries with graphitic materials. Nano Lett., 2015, 15, 7671-7677.

[39]. K. Share, A.P. Cohn, R.E. Carter, C.L. Pint. Mechanism of potassium ion intercalation staging in few layered graphene from in situ Raman spectroscopy. Nanoscale, 2016, 8, 16435-16439.

[40]. K. Share, A.P. Cohn, R. Carter, B. Rogers, C.L. Pint. Role of nitrogen-doped graphene for improved high-capacity potassium ion battery anodes. ACS Nano., 2016, 10, 9738-9744.

[41]. Z. Tai, Q. Zhang, Y. Liu, H. Liu, S. Dou. Activated carbon from the graphite with increased rate capability for the potassium ion battery. Carbon, 2017, 123, 54-61.

[42]. Li: Standard electrode potential −3.04; cationic charge +1; Faraday constant 96485.33289 C/mol; Energy per mole 293315.411986 J/mol; Atomic mass 6.94 g/mol; Energy density (mass) 42264.4685858 J/g; density 0.534 g/cm3; energy density (volumetric) 22569.2262248 J/cm3. https://en.wikipedia.org/wiki/Magnesium_battery#cite_note-li-8.

[43]. Mg: Standard electrode potential −2.372; cationic charge +2; Faraday constant 96485.33289 C/mol; Energy per mole 457726.41923 J/mol; Atomic mass 24.305 g/mol; Energy density (mass) 18832.6031364 J/g; density 1.738 g/cm3; energy density (volumetric) 32731.0642511 J/cm3. https://en.wikipedia.org/wiki/Magnesium_battery#cite_note-li-8.

[44]. C. B. Bucur, T. Gregory, A. G. Oliver, J. Muldoon. Confession of a Magnesium Battery. J. Phys. Chem. Lett., 2015, 6, 3578-3591.

[45]. S.B. Son, T. Gao, S. P. Harvey, K. X. Steirer, A. Stokes, A. Norman, C. Wang, A. Cresce, K. Xu, C. Ban. An artificial interphase enables reversible magnesium chemistry in carbonate electrolytes. Nature Chemistryvolume, 2018, 10, 532-539.

[46]. Y. Liang, R. Feng, S. Yang, H. Ma, J. Liang, J. Chen. Rechargeable Mg Batteries with Graphene-like MoS_2 Cathode and Ultrasmall Mg Nanoparticle AnodeAdv. Mater., 2011, 23, 640-643.

[47]. Z. L. Tao, L. N. Xu, X. L. Gou, J. Chen and H. T. Yuan. TiS_2 nanotubes as the cathode materials of Mg-ion batteries. Chem.Commun., 2004, 2080.

[48]. Y. Nuli, J. Yang, Y. Li and J. Wang. Mesoporous magnesium manganese silicate as cathode materials for rechargeable magnesium batteries.Chem. Commun., 2010, 46, 3794-3796.

[49]. Y. Li, Y. Nuli, J. Yang, T. Yilinuer and J. Wang. $MgFeSiO_4$ prepared via a molten salt method as a new cathode material for rechargeable magnesium batteries. Chin. Sci. Bull., 2011, 56, 386-390.

[50]. Y. Nuli, Y. Zheng, Y. Wang, J. Yang and J. Wang. Electrochemical intercalation of Mg^{2+} in 3D hierarchically porous magnesium cobalt silicate and its application as an advanced cathode material in rechargeable magnesium batteries. J. Mater. Chem., 2011, 21, 12437-12443.

[51]. T. E. Sutto and T. T. Duncan. Electrochemical and structural characterization of Mg ion intercalation into RuO_2 using an ionic liquid electrolyte. Electrochim. Acta, 2012, 79, 170-174.

[52]. S. Rasul, S. Suzuki, S. Yamaguchi and M. Miyayama. High capacity positive electrodes for secondary Mg-ion batteries. Electrochim. Acta, 2012, 82, 243-249.

[53]. D. Aurbach, Z. Lu, A. Schechter, Y. Gofer, H. Gizbar, R. Turgeman, Y. Cohen, M. Moshkovich, and E. Levi. Prototype systems for rechargeable magnesium batteries. Nature, 2000, 407, 724.

[54]. D. Aurbach, G. S. Suresh, E. Levi, A. Mitelman, O. Mizrahi, O. Chusid, M. Brunelli. Progress in Rechargeable Magnesium Battery Technology. Adv. Mater., 2007, 19(23), 4260.

[55]. Y. Mizuno, M. Okubo, E. Hosono, T. Kudo, K. Oh-ishi, A. Okazawa, N. Kojima, R. Kurono, S. Nishimura, A. Yamada. Electrochemical Mg^{2+} intercalation into a bimetallic CuFe Prussian blue analog in aqueous electrolytes. J. Mater. Chem. A, 2013, 1, 13055-13059.

[56]. S. Yagi, M. Fukuda, T. Ichitsubo, K. Nitta, M. Mizumaki, E. Matsubara. EQCM Analysis of Redox Behavior of CuFe Prussian Blue Analog in Mg Battery Electrolytes. Journal of The Electrochemical Society, 2015, 162, 12, A2356-A2361.

[57]. J. Ming, J. Guo, C. Xia, W. Wang, H. N. Alshareef. Zinc-ion batteries: Materials, mechanisms, and applications. Materials Science & Engineering R, 2019, 135, 58-84.

[58]. N. Kuperman, P. Padigi, G. Goncher, D. Evans, J. Thiebes, R. Solanki. High performance Prussian blue cathode fornonaqueous Ca-ion intercalation battery.J. Power Sources, 2017, 342, 414-418.

[59]. Y.X. Hu, D.L. Ye, B. Luo, H. Hu, X.B. Zhu, S.C. Wang, L.L. Li, S.J. Peng, L.Z. Wang. A binder-free and free-standing cobalt Sulfide@Carbon nanotube cathode material for aluminum-ion batteries. Adv. Mater., 2018, 30, 1703824.

[60]. D. A. Sverjensky, Interpretation and Prediction of Triple-Layer Model Capacitances and the Structure of the Oxide-Electrolyte-Water Interface. Geochim. Cosmochim. Acta, 2001, 65, 3643-3655.

[61]. J. Bartoll, "The early use of Prussian Blue in paintings," inProceedings of the 9th International Conference on NDT of Art, Jerusalem, Israel, May 2008.

[62]. D. Davidson, L. A. Welo. The Nature of Prussian Blue. J. Phys. Chem., 1928, 32, 8, 1191-1196.

[63]. V. D. Neff. Electrochemical oxidation and reduction of thin films of Prussian blue. J. Electrochem. Soc., 1978,125,886.

[64]. M. Giorgetti, L. Guadagnini, D. Tonelli, M. Minicucci, G. Aquilanti. Structural characterization of electrodeposited copper hexacyanoferrate films by using a spectroscopic multi-technique approach Phys. Chem. Chem. Phys., 2012, 14, 5527-5537.

[65]. J. F. Kegin, F. D. Miles. Structure and formula of prussian blue and related compound. Nature, 1936, 137, 577.

[66]. M. Giorgetti, M. Berrettoni, A. Filipponi, P. J. Kulesza, R. Marassi. Evidence of four-body contributions in the EXAFS spectrum of $Na_2Co[Fe(CN)_6]$. Chemical Physics Letters, 1997, 275, 108-112.

[67]. C. G. Tsiafoulis, P. N. Trikalitis, M. I. Prodromidis. Synthesis, characterization and performance of vanadium hexacyanoferrate as electrocatalyst of H_2O_2. Electrochemistry Communications, 2005, 7, 1398-1404.

[68]. T. Shibata, Y. Moritomo. Ultrafast cation intercalation in nanoporous nickel Hexacyanoferrate. Chem. Commun., 2014, 50, 12941.

[69]. M. Takachi, Y. Fukuzumi, Y. Moritomo. Na+ diff usion kinetics in nanoporous

metalhexacyanoferrates. Dalton Trans., 2016, 45, 458.

[70]. L. Wang, J. Song, R. Qiao, L. A. Wray, M. A. Hossain, Y.D. Chuang, W. Yang, Y. Lu, D. Evans, J. Lee, S. Vail, X. Zhao, M. Nishijima, S. Kakimoto, J. B. Goodenough. Rhombohedral Prussian White as Cathode for Rechargeable Sodium-Ion Batteries. J. Am. Chem. Soc., 2015, 137, 2548-2554.

[71]. L. Wang, Y. Lu, J. Liu, M. Xu, J. Cheng, D. Zhang, J. B. Goodenough. A Superior Low-Cost Cathode for a Na-Ion Battery. Angew. Chem.Int. Ed., 2013, 52, 1964.

[72]. X. Wu, C. Wu, C. Wei, L. Hu, J. Qian, Y. Cao, X. Ai, J. Wang, H. Yang. Highly Crystallized $Na_2CoFe(CN)_6$ with Suppressed Lattice Defects as Superior Cathode Material for Sodium-Ion Batteries. ACS Appl. Mater. Interfaces 2016, 8, 5393.

[73]. H. W. Lee, R. Y. Wang, M. Pasta1, S. W. Lee, N. Liu, Y. Cui. Manganese hexacyanomanganate open framework as a high-capacity positive electrode material for sodium-ion batteries. Nat Commun., 2014,14, 5, 5280. doi: 10.1038/ncomms6280.

[74]. O. Makowski, J. Stroka, P. J. Kulesza, M. A. Malik, Z. Galus. Electrochemical identity of copper hexacyanoferrate in the solid-state:evidence for the presence and redox activity of both iron and copper ionic sites. Journal of Electroanalytical Chemistry, 2002, 532, 157-164.

[75]. D. Shaojun, L. Fengbin. Researches on chemically modified electrodes: Part XV. Preparation and electrochromism of the vanadium hexacyanoferrate film modified electrode. J. Electroanal. Chem. Interfacial Electrochem., 1986, 210, 31-44.

[76]. A. Dostal. Festko¨rperreaktionen an metallhexacyanometallat-modifiziertem Elektroden. Dr. Diss. Math. Fak. I der Humboldt-Universita¨t zu Berlin (1998).

[77]. A. Mullaliu, G. Aquilanti, P. Conti, J. R. Plaisier, M. Fehse, L. Stievano, M. Giorgetti. Copper Electroactivity in Prussian Blue-Based Cathode Disclosed by Operando XAS. J. Phys. Chem. C, 2018, 122, 15868-15877.

[78]. A. Mullaliua, M. T. Sougrati, N. Louvain, G. Aquilanti, M. L. Doublet, L. Stievano, M. Giorgetti. The electrochemical activity of the nitrosyl ligand in copper nitroprusside: a new possible redox mechanism for lithium battery electrode materials? Electrochimica Acta, 2017, 257, 364-371.

[79]. S. Guo, J. Yi, Y. Sun, H. Zhou. Recent advances in titanium-based electrode materials for stationary sodium-ion batteries. Energy Environ. Sci., 2016, 9, 2978-3006.

[80]. R.S. Nicholson. Theory and Application of Cyclic Voltammetry for Measurement of Electrode Reaction Kinetics. Anal. Chem., 1965, 37,11, 1351-1355. doi:10.1021/ac60230a016.

[81]. Y. F. Pulido, C. Blanco, D. Anseán, V. M. García, F. Ferrero, M. Valledor. Determination of suitable parameters for battery analysis by Electrochemical Impedance Spectroscopy. Measurement, 2017, 106,1-11.

[82]. S. Adak, L. Daemen, M. Hartl, D. Williams, J. Summerhill, H. Nakotte. Thermal expansionin 3d-metal Prussian Blue Analogs-A surveystudy. Journal of Solid State Chemistry, 2011, 184, 2854-2861.

[83]. M. Avila, L. Reguera, J. Rodrı´guez-Herna´ndez, J. Balmaseda, E. Reguera. Porous framework of $T_2[Fe(CN)_6]\cdot xH_2O$ with T ¼ Co, Ni, Cu, Zn, and H_2 storage Journal of Solid State Chemistry, 2008, 181, 2899-2907.

[84]. J. Rodríguez-Hernández, L. Reguera, A.A. Lemus-Santana, E. Reguera. silver nitroprusside: a typical coordination within the metal nitroprusside series. Inorganic Chemical Acta, 2015, 428, 51-56.

[85]. D. Horley, E. G. Torrible. The infrared spectra of some titanium complexes with primary diamines. Canadian Journal of Chemistry, 1965, 43, 3201-3205.

[86]. V. Luca, S. Djajanti, R. F. Howe. Structural and Electronic Properties of Sol-Gel Titanium Oxides Studied by X-ray Absorption Spectroscopy. J. Phys. Chem. B, 1998, 102, 10650-10657.

[87]. B. Paulitsch, J. Yun, A. S. Bandarenk. Electrodeposited $Na_2VO_x[Fe(CN)_6]$ films As a Cathode Material for Aqueous Na-Ion Batteries. ACS Appl. Mater. Interfaces, 2017, 9, 8107-8112.

[88]. Y. Luo, B. Shen, B. Guo, L. Hu, Q. Xu, R. Zhan, Y. Zhang, S. Bao, M. Xu. Potassium titanium hexacyanoferrate as a cathode material for potassiumion Batteries. Journal of Physics and Chemistry of Solids, 2018, 122, 31-35.

[89]. M. Xie, Y. Huang, M. Xu, R. Chen, X. Zhang, L. Li, F. Wu. Sodium titanium hexacyanoferrate as an environmentally friendly and low-cost cathode material for sodium-ion batteries. Journal of Power Sources, 2016, 302, 7-12.

[90]. S. Yagi, M. Fukuda, R. Makiura, T. Ichitsubo, E. Matsubara. EQCM analysis of redox behavior of Prussian blue in a lithium battery electrolyte. J. Mater. Chem. A, 2014, 2, 8041-8047.

[91]. R. Brydsoni, H. Sauer, W. Engel, J. M. Thomas, E. Zeitler, N. Kosugill, H. Kurodall. Electron energy loss and x-ray absorption spectroscopy of rutile and anatase: a test of structural sensitivity. Condens. Matter l, 1989, 797-812.

[92]. S. Abdoun. Electrochemical methods of analysis. https://www.slideshare.net/SihamAbdallaha/electrochemical-method-of-analysis-31352857.

[93]. D. Wardecki, D. O. Ojwang, J. Grins, G. Svensson. Neutron Diffraction and EXAFS Studies of $K_{2x/3}Cu\ [Fe\ (CN)_6]_{2/3}\cdot nH_2O$. Cryst. Growth Des., 2017, 17, 1285-1292.

Appendix A

Operating parameters:

Capacity (Ah): is the total quantity of charge that the battery may deliver in discharge.

1Ah = 3600 C

Specific capacity (Ah/kg): is the total quantity of charge that the battery may deliver in dischargeper weight unit.

Capacity density (Ah/cm^3): is the total quantity of charge that the battery may deliver in discharge per volume unit.

Energy (Wh): The theoretical available energy for 1 mol of reaction. In Wh (Watt hours) 1 Wh = 3600 J

Specific energy (Wh/kg): or **gravimetric energy density** is the maximum (theoretical) energy that the battery can deliver per weight unit.

Energy density (Wh/cm^3): or **volumetric energy density** is the maximum (theoretical) energy that the battery can deliver per volume unit.

Power P = E i (in W = J s). In analogy we can define the Specific power W/Kg and the Power Density in W/cm^3

Appendix B:

Table 7. Mass of pellets we used in KNO3 Electrolyte for the repeat test

KNO3 Electrolyte		
Repeat time	Pellet (mg)	AM (mg)
1	1.60	1.12
2	1.12	0.78
3	1.16	0.81

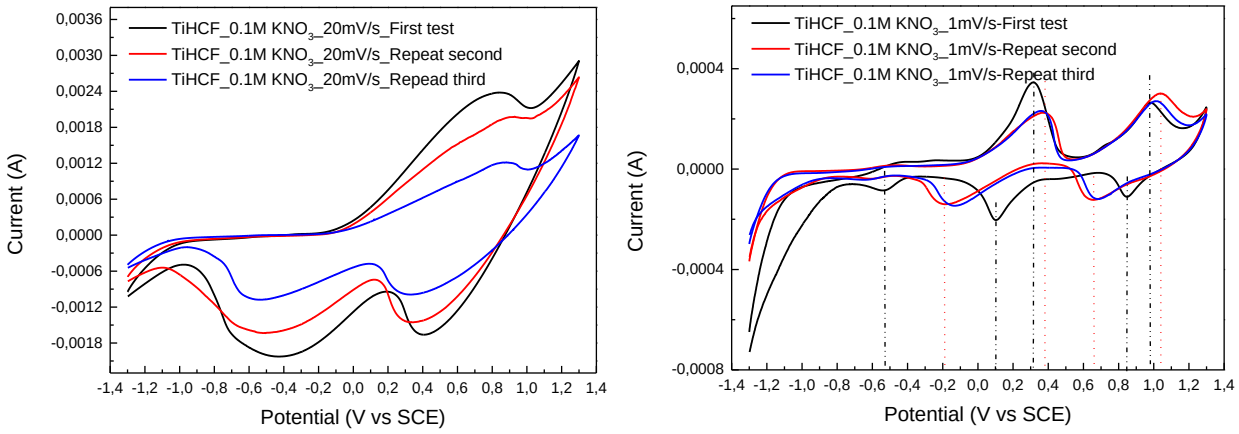

Figure 34. Repeated test of Cyclic voltammetry in 0.1M KNO_3 electrolyte

Appendix C:

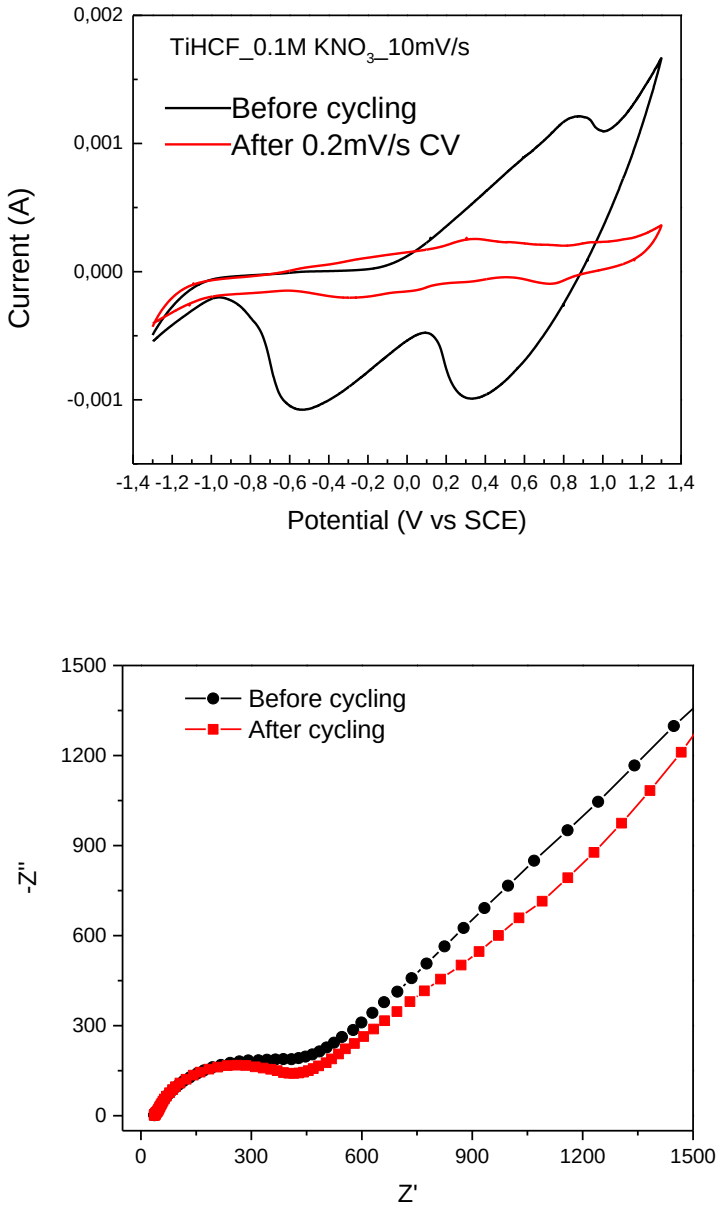

Figure 35. CV and EIS test in 0.1M KNO_3 electrolyte before and after cycling

Appendix D:

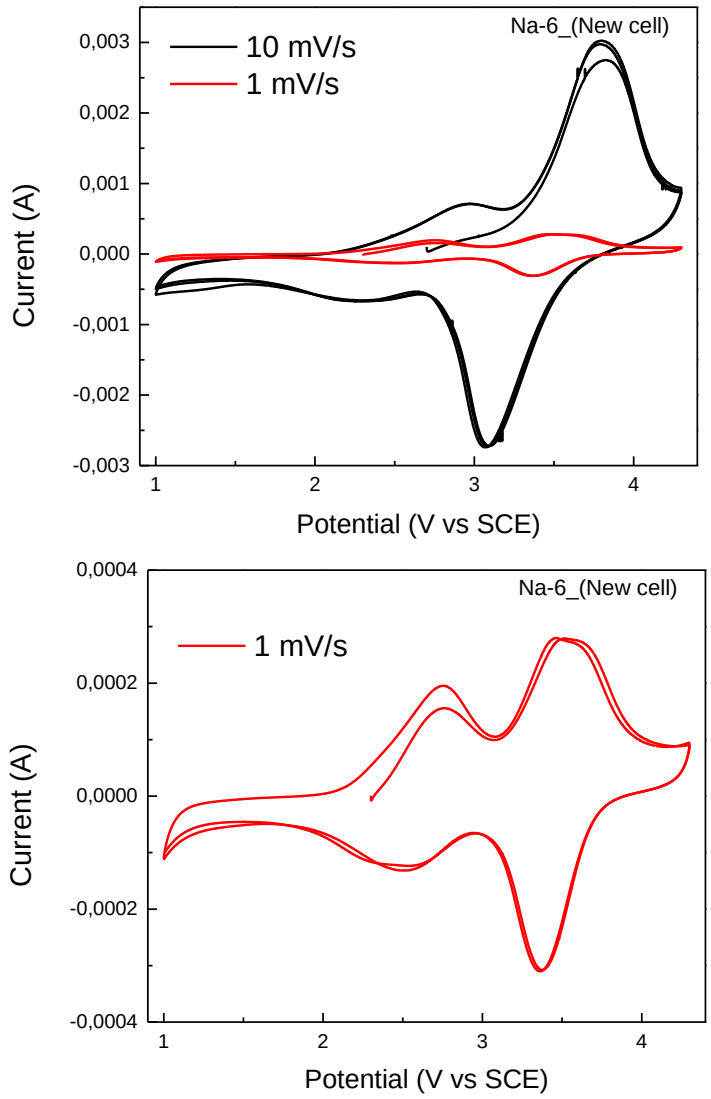

Figure 36. Cyclic voltammetry of Na-ion coin cells at voltage range: 1-4.2V.

Appendix E:

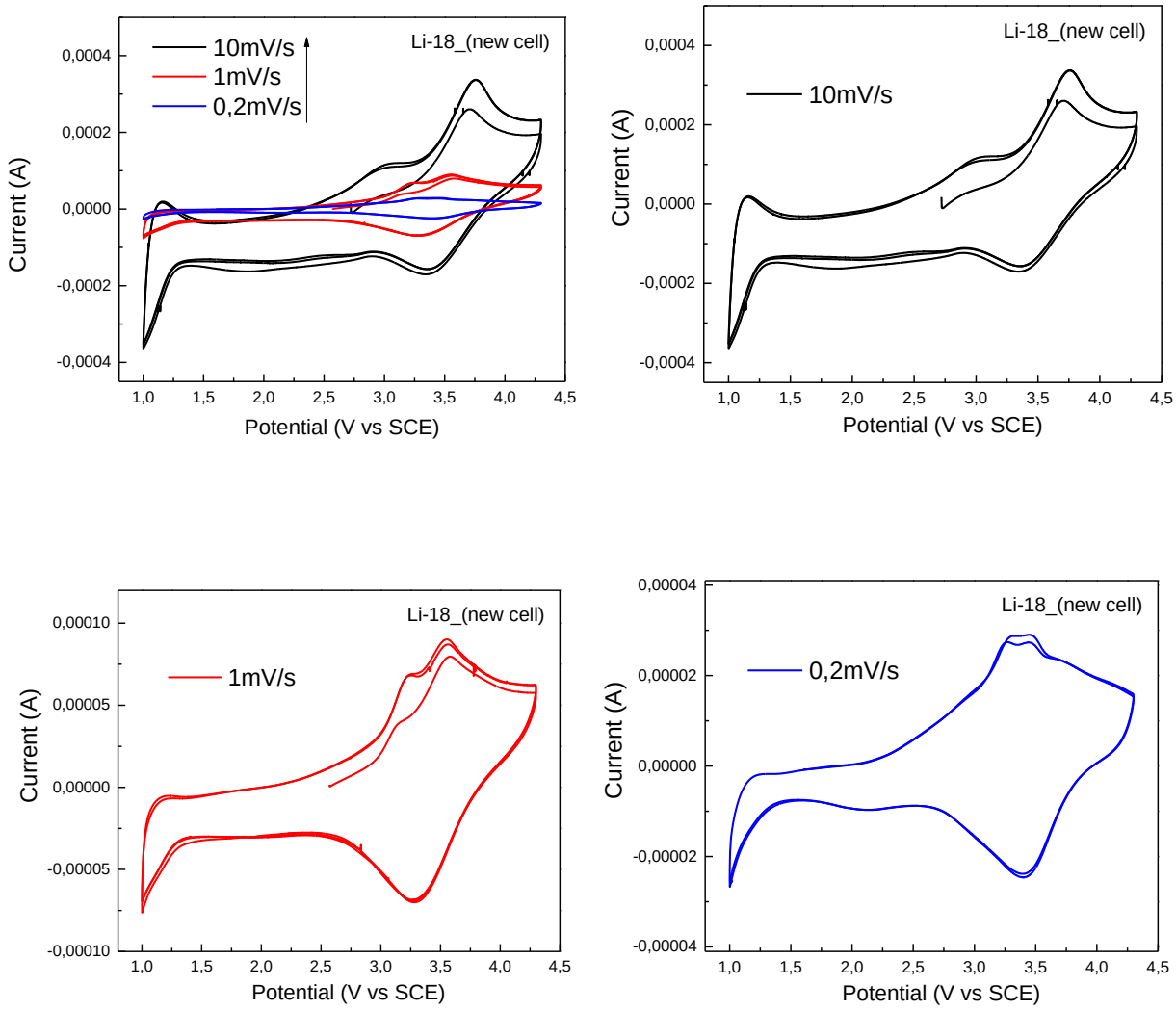

Figure 37. Cyclic voltammetry of Li-ion coin cells at voltage range: 1-4.2V.

Appendix F:

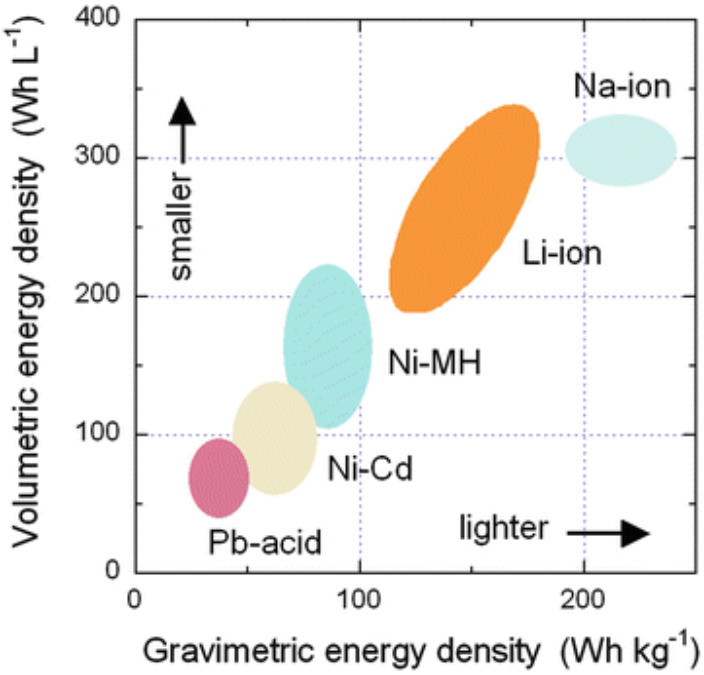

Figure 38. Specific energy and specific power plot of energy storage and conversion devices.

Acknowledgement

Time flies. Two years master studing is coming to an end. I'm glad that I joined this Master program-Advanced Spectroscopy Chemistry (ASC), and I also appreciate the help and kindness of everyone I met during this process.

Two years ago, I started my study in france, a totally different country with my hometown. At the begining, I really apprecaite the help and kindness of Francine Chanier and Aude Zeglin, the secrataries of ASC office. They offer us help whenever we ask for, and make us enjoy the whole study period. In addition, I do want to thank Prof. Sylvain Cristol and Cédric Lion, they paid great effort to organize our study program and gave us advice about our study plan. I'm lucky and happy that I moved to bologna for the second year and found a great lab there by listening of their suggestion.

I'm so glad that I found a lovely lab and to work with people who are so kind, warmhearted and also so passionate about research jobs. I want to thank my professor: Prof. Marco Giorgetti. I'm so appreciate you accepted me in the lab, and offering me the great chance to study there (even the study experience in synchrotron lab). And thank you so much for your guidance and patience during the process of correction of my master thesis. I learn a lot from your not only the theoretical knowledge, but also the way to do things.

In addition, I do want to thank the people in my lab. Doctor Angelo mullaliu, thank you for your support and concern during the whole process of my internship and master thesis. Your kindness, your passion about research encourage me to go on my study. Doctor Elisa Musella, thank you for your kindness and help, concern during the past year, happy to see your cheerful smile everyday. I also want to thank Doctor Federica Mariani, Prof. Isacco Gualandi, thank you so much for the help you offered during my experiment, and Prof. Domenica Tonelli, thank you the warm greating everyday.

I want to thank all our bologna ASC fellow: Alberto Manchado Parra, Carolina A. Garcia, Ffy Panukorn, Nicola poli, Ornella Laouadi. Because of you, i'm not alone here. And I appreciate and cherish the time we spend together. You are my family here.

At last, I want to say thanks to my family: my mother, father, brother and sister-in-law. Without your support, I cannot follow my dream, do the things I want to do. I love you so much.

Min Li

07/2019